NASA Technical Memorandum 81929

Operating Characteristics of the Langley Mach 7 Scramjet Test Facility

Robert W. Guy, Marvin G. Torrence,
Alexander P. Sabol, and James N. Mueller

MARCH 1981

NASA Technical Memorandum 81929

Operating Characteristics of the Langley Mach 7 Scramjet Test Facility

Robert W. Guy, Marvin G. Torrence,
Alexander P. Sabol, and James N. Mueller
Langley Research Center
Hampton, Virginia

National Aeronautics
and Space Administration

**Scientific and Technical
Information Branch**

1981

SUMMARY

Operating characteristics of the Langley Mach 7 Scramjet Test Facility are described. The facility is designed for testing airframe-integrated scramjet (supersonic combustion ramjet) engine models and has certain features not usually required in conventional aerodynamic wind tunnels. These features include duplication of the flight Mach number total enthalpy, flight altitude simulation, and simulation of engine-airframe integration effects such as vehicle bow-shock wave precompression and boundary-layer ingestion by the engine. Data obtained during facility calibration and during tests of a hydrogen-burning, airframe-integrated scramjet are discussed. An adverse interaction between the facility flow and the scramjet-engine flow during combustion of the fuel is described, and a solution to this problem is presented. Nominal stagnation conditions of the electric-arc-heated airflow were 2.89 MN/m^2 (28.5 atm) and 2180 K (3925°R), and the free jet exit Mach number was 6.08.

INTRODUCTION

The airframe-integrated scramjet (supersonic combustion ramjet) (fig. 1) is the subject of extensive research at NASA Langley Research Center. Analytical studies (refs. 1 and 2) have indicated that this fixed-geometry, hydrogen-burning engine has potential for high thrust and efficiency with low drag, weight, and cooling requirements, especially at flight Mach numbers above 6. Other analytical studies (refs. 3 and 4) have explored the structural and regenerative cooling systems necessary for flight-weight scramjets of this type. Experimental research is currently in progress using subscale, boilerplate engines in wind-tunnel facilities adapted to airframe-integrated scramjet research. Two hydrogen-burning engine models have been fabricated (ref. 5), and initial tests have been conducted in ground facilities at conditions simulating flight at Mach numbers near 4 and 7. (See ref. 6.)

The ground facilities used in these tests are unique in that certain features must be included which are usually unnecessary in conventional aerodynamic test facilities. First, the air total enthalpy corresponding to the flight Mach number has to be duplicated and a reasonable flight altitude simulated so that pressures, temperatures, and velocities in the scramjet combustor duplicate flight conditions. Second, simulation of the integration of the engine with the flight vehicle must be achieved. This is accomplished by simulating the aircraft bow-shock precompression and the ingestion of the vehicle undersurface boundary layer. The shock precompression is simulated by testing at a scramjet inlet Mach number (i.e., the facility nozzle exit Mach number) which duplicates the Mach number after the bow-shock precompression of a vehicle forebody but at an airflow total temperature which duplicates the flight Mach number total enthalpy. Flight engine boundary-layer ingestion is simulated by mounting the scramjet model in the test section such that a portion of the facility nozzle boundary layer is ingested by the model.

The aft undersurface of the flight vehicle provides a portion of the engine exhaust nozzle, but no simulation of this configuration was attempted during the present tests. The ratio of the exit area to the inlet area of a typical scramjet engine is 3.5, but, without vehicle undersurface simulation in ground facility tests, this area ratio has been unity. Size of the test engines is limited by facility size, mass flow-rate capability, and dc power supply available to heat the test air to the desired total enthalpy.

This report is concerned with the Langley Mach 7 Scramjet Test Facility, at which the initial tests of the airframe-integrated scramjet model were conducted. This is an electric-arc-heated facility capable of nominal airflow test conditions duplicating Mach 7 flight enthalpy and simulating an altitude of 35.14 km (115 300 ft). Nominal real-gas stagnation conditions during the experimental program were 2.89 MN/m^2 (28.5 atm) and 2180 K (3925°R), and the free jet exit Mach number was 6.08. The unique relationship between the scramjet model and the test facility created problems not usually encountered in wind-tunnel tests of aerodynamic models. One such problem was an interaction between the facility and the model when hydrogen fuel was injected into the engine airflow. This interaction caused increased scramjet drag as well as inlet unstarts at the higher fuel flow rates.

The operating characteristics of the Langley Mach 7 Scramjet Test Facility are discussed in this report. The facility and the scramjet model are described, facility performance is documented, and the facility-model interaction and the techniques used to minimize it are discussed.

SYMBOLS

Dimensional quantities are presented in both the International System of Units (SI) and U.S. Customary Units. Measurements and calculations were made in U.S. Customary Units.

A_c scramjet inlet area normal to flow direction

c_p specific heat at constant pressure

$C_{D,1}$ fuel-off scramjet drag coefficient, $\frac{D}{q_1 A_c}$

D fuel-off scramjet drag

E arc voltage

F axial force on scramjet

h enthalpy

H scramjet inlet height

I arc current

$\dot{m}$	mass flow rate
$\dot{m}_t$	total facility air mass flow rate ($\dot{m}_1 + \dot{m}_{ph}$)
M	Mach number
p	pressure
q	dynamic pressure
$\dot{q}$	heat transfer rate per unit area
$\dot{Q}$	cooling-water heat transfer rate
r_{eff}	effective radius
R_1	unit Reynolds number at facility nozzle exit
s'	axial distance from scramjet sidewall leading edge (fig. 17)
T	temperature
V	velocity
x	distance in axial direction
y	distance in vertical direction
γ	ratio of specific heats
ΔF	change in engine force from fuel-off to fuel-on condition
ΔT	change in exit cooling-water temperature between arc-off and arc-on conditions
ρ	density
ϕ_{inj}	injected fuel equivalence ratio

Subscripts:

arc	electric arc
arc air	air which passes through electric arc
byp air	bypass air added downstream of arc heater
c	peripheral nozzle
cabin	test cabin in which model is mounted
DE	downstream electrode

h	hot-flow nozzle
H_2O	cooling water
ph	peripheral-nozzle airflow
PL	plenum
PR	plenum rings
run	during arc-on
start	prior to arc-on, but with facility air flowing
t,1	facility stagnation condition
t,2	stagnation condition behind normal shock
TH	throat of nozzle
UE	upstream electrode
∞	free-stream static conditions ahead of aircraft bow-shock wave
1	static conditions upstream of scramjet inlet and at facility nozzle exit

LANGLEY MACH 7 SCRAMJET TEST FACILITY

The Langley Scramjet Test Facility (STF) is an electric-arc-heated facility with air as the test gas. Approximately one-third of the facility airflow passes through the heater; the remainder is added downstream of the heater. From this mixing chamber, the test air is expanded in a contoured nozzle to the test section where it exits as a free jet. The flow is then diffused to a subsonic velocity, cooled by an aftercooler, and exhausted to a vacuum sphere. A history and general description of the STF is given in reference 7. Figure 2 is a scaled elevation view of the tunnel circuit; figure 3 is a schematic of the test set-up; and figure 4 is a photograph of the arc heater, nozzle, test section, and model. A brief description of the present facility configuration is presented in the following section.

Major Support Systems

A schematic of the major support systems required for conducting scramjet engine tests in the STF is shown in figure 5. These systems include high-pressure air, electrical power for the arc heater, high-pressure deionized cooling water, vacuum system, hydrogen fuel system, and model injection system.

Air.- Three high-pressure air lines enter the STF. All come from a 34.58-MN/m^2 (5000-psig) bottle field and are regulated to the desired supply

pressure at the facility. The air line labeled "A" in figure 5 supplies air to the arc heater at a nominal flow rate of 0.73 kg/s (1.62 lbm/s). Line "B" supplies bypass or mixing air which enters the flow just downstream of the heater. This unheated air is used to dilute the arc-heated flow to obtain the desired total enthalpy. The nominal value of this bypass airflow during the scramjet tests was 1.56 kg/s (3.45 lbm/s).

Air from the line labeled "C" does not enter the heated flow nozzle. Instead, it flows as unheated air through a peripheral nozzle which enshrouds the hot-flow nozzle on the sides and bottom (fig. 3). Flow rates through this line could be as high as 9.07 kg/s (20 lbm/s), but they were varied during the tests as is discussed subsequently.

Electrical power.- Electric power to heat the air in the electric arc is provided by two 10-MW power supplies connected in series so that up to 20 MW of dc power is available in the arc-heater circuit. Each power supply consists of an array of ac transformers and silicon diode rectifiers. About one-half of the available power is dissipated in ballast resistors, which are necessary to achieve arc stability. During the tests, the total ballast resistance was varied from 1.53 ohms to 1.67 ohms. Nominal voltage across the arc was 4440 volts at a current of 2200 amperes for a nominal arc power of 9.77 MW.

Cooling water.- Arc-heater components, the plenum chamber, and the throat are cooled with deionized water (Resistivity ≈ 300 000 ohm-cm) from a tank capable of storing 189 271 L (50 000 gal). A pump driven by a 2.24-MW (3000-hp) motor supplies the water to the components at pressures up to 9.75 MN/m^2 (1400 psig). Supply manifold pressure during the scramjet tests was 7 MN/m^2 (1000 psig), and return manifold pressure was approximately atmospheric. Total flow to all components was 66.88 L/s (1060 gal/min).

Vacuum.- The airflow from the facility exhausts into a 30.48-m (100-ft) diameter vacuum sphere. The sphere is isolated from the tunnel circuit by a 91.44-cm (36-in.) diameter butterfly valve. Prior to a scramjet test, the sphere was evacuated to 138 N/m^2 (0.020 psia) by a three-stage steam ejector. The steam ejector uses 3.28 kg/s (26 000 lbm/hr) of steam when all three stages are in operation.

Hydrogen fuel.- Gaseous hydrogen is supplied to the scramjet engine from a 0.89-m^3 (31.46-ft^3) storage bottle located on the roof of the building above the engine. Maximum bottle pressure during the test series was 4.93 MN/m^2 (700 psig). This bottle is recharged as required through a 6.35-mm (0.25-in.) diameter line from remotely located trailers.

The control valves for the hydrogen system are also located on the roof. The hydrogen flows through a continuous line (welded joints) in the test room into an instrumentation box above the test section and is injected from the three instream struts in the scramjet. Fuel flow is controlled automatically during a test by a cam-type control unit at preselected flow rates, or the fuel flow can be varied continually by manually controlling the regulated supply pressure. Fuel lines were purged with gaseous nitrogen before and after each test as a safety measure.

Model injection.- A hydraulic model injection system is located in the instrumentation box above the test section. The model is injected after tunnel flow is established in order to protect model heat-transfer gauges during arc initiation. The stroke of the injection cylinder is 30.48 cm (12 in.). The hydraulic supply pressure can be varied up to 20.79 MN/m^2 (3000 psig), and the model insertion rate is directly proportional to this pressure. During these tests, the hydraulic pressure was 5.62 MN/m^2 (800 psig), which resulted in an injection time of 2.5 seconds with a 11.77 m/s^2 (38.60 ft/s^2) acceleration. The last 1.27 cm (0.5 in.) of travel was used to cushion the injection. Removable shims on the injection cylinder permitted the injected position of the engine relative to the facility nozzle exit to be changed as required from run to run.

Tunnel System

Arc heater.- The test stream is heated to the desired stagnation condition with an electric arc. This arc heater consists of two coaxial cylindrical copper electrodes (fig. 6) separated by an electrically insulated air-inlet chamber. It is similar in design to the arc heater described in reference 8. The upstream electrode (the anode) is 61.29 cm (24.13 in.) long with an inner diameter of 9.7 cm (3.82 in.) and an outer diameter of 11.43 cm (4.50 in.). The upstream end of this electrode is closed. The downstream electrode (the cathode) is 108.43 cm (42.69 in.) long with an inner diameter of 5.89 cm (2.32 in.) and an outer diameter of 7.32 cm (2.88 in.). The heater was operated during the present tests with the upstream electrode nominally 2390 volts above ground and the downstream electrode 2050 volts below ground. This necessitated insulating both electrodes from ground. A 0.89-mm (0.035-in.) diameter steel rod was used initially between the electrodes as a starter to establish the arc. Water-cooled magnetic-field coils help to stabilize the arc and limit the arc length to approximately 137.16 cm (4.5 ft). The air through the arc is swirled tangentially into the air-inlet chamber between the two electrodes from twenty 1.85-mm (0.073-in.) diameter orifices. This swirl, together with swirl created by the interaction of the electric arc with the magnetic field, rotates the arc for increased arc stability and also spreads the intense heating rate of the arc attachment region over a greater electrode surface area. The arc heater operated in a dependable manner during this test series with few problems.

Air, flowing at a rate of 0.73 kg/s (1.62 lbm/s), was heated by the arc to an enthalpy of approximately 8.11 MJ/kg (3490 Btu/lbm) and an associated temperature of 4722 K (8500°R) at the exit of the downstream electrode (fig. 6). At this location, 1.56 kg/s (3.45 lbm/s) of room-temperature air was injected radially into the arc-heated air from twenty-four 3.56-mm (0.140-in.) by 1.65-mm (0.065-in.) rectangular slots located between rings 1 and 2 and rings 2 and 3 of three plenum rings which are used to increase the inner diameter from that of the downstream electrode (5.89 cm (2.32 in.)) to that of the plenum chamber (26.35 cm (10.38 in.)). (See fig. 7.) This mixing scheme was necessary to obtain the test total enthalpy because the arc heater could not process the total facility mass flow rate without arc blowout. The resulting mixture, after plenum and throat losses were subtracted, had a nominal total enthalpy of 2.51 MJ/kg (1080 Btu/lbm) and a temperature of 2180 K (3925°R). At a flow rate of 2.30 kg/s (5.07 lbm/s), the hot-test gas passed through the 3.56-mm (0.140-in.) by 24.13-cm (9.5-in.) throat of the two-dimensional, contoured noz-

zle, which produced a free jet exit flow at Mach 6.08 and a nominal stagnation pressure of 2.89 MN/m^2 (28.5 atm).

Facility nozzles.- The test air, which was heated to a Mach 7 enthalpy level, was expanded from the plenum chamber through the two-dimensional contoured nozzle (fig. 8), which was designed for a Mach 6 exit flow. (The nozzle was designed for a total pressure of 3.04 MN/m^2 (30 atm) and a total temperature of 2222 K (4000°R), with the assumption that the flow was chemically frozen but in vibrational equilibrium.) This technique simulated the aircraft bow-shock wave precompression of a vehicle flying at Mach 7 with a Mach 6 flow at the scramjet inlet. Assuming equilibrium flow (effects of frozen chemistry are negligible), the nominal exit Mach number for the conditions of this test series was 6.08. The top and bottom surfaces of the nozzle are contoured and all four surfaces were corrected for boundary-layer growth. The nozzle geometric exit area was 30.48 cm (12 in.) high by 27.18 cm (10.7 in.) wide (calculated boundary-layer displacement thickness at the exit is about 1.52 cm (0.6 in.)).

As shown in figures 3 and 8, a second peripheral nozzle is used to expand unheated air along the sides and bottom of the hot-flow nozzle. The exit height of this nozzle was 13.97 cm (5.5 in.) and the nozzle exit Mach number was 3.85. The purpose of this peripheral flow was to permit testing of larger models by increasing the usable cross-sectional area of the center-heated flow without the necessity of heating a larger supply of air. The intent was to match the static pressures at the exits of the hot-flow and peripheral-flow nozzles so that no disturbance (wave) would originate at this juncture which could affect engine performance. With this technique, any disturbances would occur at the outer perimeter of the peripheral-flow nozzle, thus effectively enlarging the usable hot-flow field. Design considerations for this type of hot-core nozzle concept are presented in reference 9.

During the experimental program, tests were conducted with the exit pressures of the two flows unmatched. Nozzle extensions (fig. 3) were then added to prevent nozzle-exit disturbances from entering the scramjet inlet. This aspect is discussed in more detail in a subsequent section.

Test section, diffuser, and aftercooler.- After exiting the hot-flow nozzle at Mach 6.08 as a free jet, the test air flowed over and through the scramjet model, which was mounted in the 1.22-m (4-ft) diameter test section. In order to simulate the boundary-layer ingestion associated with engine-airframe integration, the engine was aligned with the top surface of the hot-flow nozzle as shown in figure 3. Thus, the facility-nozzle top-surface boundary-layer air was ingested by the engine model. This simulated the ingestion of the aircraft forebody boundary layer by a flight engine. The remaining three sides of the engine inlet did not ingest any facility-nozzle boundary-layer air.

As the flow passes through the 1.22-m (4-ft) diameter, 10.24-m (33.6-ft) long, straight-pipe diffuser section downstream of the test section (fig. 2), mixing occurs between the hot flow from the facility nozzle, the engine exhaust gases, the unheated peripheral nozzle flow, and the surrounding ambient air. Downstream of the straight-pipe section, the diffuser expands in a conical section 7.44 m (24.4 ft) long to a diameter of 3.00 m (9.83 ft). The large-diameter section contains an aftercooler (air-to-water heat exchange) consist-

ing of 676 finned, 4.83-cm (1.9-in.) diameter cooling-water tubes. The finned sections of the cooling-water tubes are 1.83 m (6 ft) long with 338 180° bends (one bend joining each pair of tubes) facing the oncoming flow. This aftercooler cools the tunnel flow to approximately 361 K (650°R) prior to its entry into the 30.48-m (100-ft) diameter vacuum sphere.

Facility Instrumentation and Data Reduction

The facility was instrumented with 45 sensors. Pressures were measured in the arc heater, plenum chamber, test section, diffuser, and vacuum sphere. Pressures were also measured at the nozzle exits and downstream of the aftercooler. To characterize the flow upstream of the nozzle throat, an energy balance on the airflow through the arc heater and plenum chamber was performed. To accomplish this, it was necessary to measure arc voltage, arc current, cooling-water flow rates and temperature increases ΔT, and heater and bypass airflow rates. Facility data were recorded on a magnetic tape system at a rate of 200 points per channel per second.

After a test, the magnetic tape from the 45-channel data system was transported to Langley's central computer center. These data were then reduced to facility pressures, temperatures, volume flow rates, etc., using preprogrammed calibrations. In addition, existing software was used to calculate various parameters such as mass flow rates, total enthalpy, arc-heater component heat losses, etc. All data were tabulated as a function of time, and selected parameters were plotted as functions of time.

SCRAMJET MODEL

The scramjet model which was used in the test series is shown in figure 9. The external cover plates have been removed to reveal instrumentation leads and cooling-water lines (fig. 9(a)). The engine model was constructed entirely of oxygen-free, high-conductivity copper and weighed 272 kg (600 lb). It was heat-sink cooled except for water cooling in high heat-flux areas such as leading edges, fuel-injection struts, and portions of the combustor. Design details of the model are contained in reference 5.

The model has a projected inlet height of 20.32 cm (8 in.) and an inlet width of 16.26 cm (6.4 in.); overall length of the engine is 151 cm (59.5 in.). Sidewall leading edges and fuel-injection struts are swept at 48°, and the bottom of the inlet is open to permit flow spillage for easier inlet starting. At an inlet Mach number of 6, 94 percent of the airflow approaching the inlet is captured, the effective inlet contraction ratio is 7.4, the inlet total-pressure recovery ratio is 0.65, and the scramjet combustor entrance Mach number is 3.1. (See ref. 10). The scramjet-engine nozzle exit area is equal to the inlet area; that is, there is no simulation of the nozzle extension along the vehicle afterbody.

Hydrogen fuel is introduced into the engine from three instream struts (fig. 9(b)) which serve to complete the inlet compression process as well as to provide additional surfaces for fuel injection. Fuel injection from dis-

crete sonic orifices in various combinations perpendicular and parallel to the air stream (as indicated in fig. 1) can be employed. The majority of the tests reported herein were conducted with all-perpendicular fuel injection. This was done because of the potential for higher performance at this Mach number with the more rapid mixing obtained with all-perpendicular fuel injection. Stoichiometric hydrogen fuel injection for the nominal test condition was 0.0276 kg/s (0.0609 lbm/s).

Engine internal instrumentation consisted of 93 static-pressure orifices, 46 Gardon-type (ref. 11) heat-transfer gauges, and 106 chromel-alumel thermocouples. External instrumentation consisted of static-pressure taps located on the sidewall and cowl forward-facing surfaces, the underside of the inlet sidewalls, the base of the engine, and the top of the engine. The model was also mounted on a one-component force balance to measure thrust or drag.

Data were recorded at a rate of 10 measurements per channel per second on a 217-channel system wired directly into Langley's central computer system. The data were reduced to pressure, temperature, heating rates, fuel flow rates, model force, etc., using existing software. All reduced data were returned to the test engineer tabulated as a function of time with selected parameters plotted as a function of time.

TEST PROCEDURE

A prerun checklist is used to set up the various systems in the Langley Mach 7 Scramjet Test Facility (STF) such as air, electrical power, cooling water, vacuum, hydraulics, hydrogen fuel, and data acquisition. At the point in the checklist where the tunnel circuit pressure had been lowered to less than 689 N/m^2 (0.100 psia), a "wind-off" data zero from the force balance was recorded while the scramjet model was in the normal test position. At the same time, data zeroes were recorded from the model pressure transducers which were exposed (on a separate vacuum system) to a pressure less than 14 N/m^2 (0.002 psia). All pressure transducers were then calibrated against the reading of a quartz-crystal pressure standard.

After the prerun checklist was completed, a check run was made in the facility with all systems functioning except electrical power, hydrogen fuel, movie cameras, and the data systems. Although these systems were not in operation, the timing of the sequencers controlling them and all other systems were checked during this period. If all systems performed as expected during the check run, final preparations for a "hot" test were completed.

After cooling water was brought on manually, a switch was activated, and the subsequent hot-test sequence of events was completely automatic. These events were controlled by three cam systems, an autosequencer, and several timers, all of which were preprogrammed. The test sequence was as follows:

(1) Data systems on

(2) Cameras on

(3) Airflow on

(4) Prepurge hydrogen lines with nitrogen

(5) Electric arc on

(6) Inject scramjet model into test stream

(7) Obtain fuel-off scramjet data

(8) Hydrogen fuel on

(9) Obtain fuel-on scramjet data

(10) Hydrogen fuel off

(11) Postpurge hydrogen lines with nitrogen

(12) Electric arc off

(13) Airflow off

(14) Cameras off

(15) Data systems off

(16) Retract model

Arc-on test times during this test series ranged up to 25 seconds. After the test, the cooling-water flow was terminated and a postrun checklist was used to secure all facility systems.

FACILITY PERFORMANCE

Total Enthalpy

Total enthalpy measurement in a hot-flow facility such as the STF, where total temperatures can range up to 2222 K (4000°R), is a difficult task. Any enthalpy determination technique must be examined carefully, relative to the particular facility flow situation, in order to assess its potential accuracy. Four methods have been used to determine total enthalpy in the STF. These are the energy balance technique, the equilibrium sonic-throat method, a total-temperature probe, and measurements of test-stream pitot pressure and stagnation-point heating rate.

Energy balance.- The energy-balance technique can be expected to yield reasonably accurate values of total enthalpy when applied to the STF arc heater because of the high efficiency of the heater (~55 percent). The flow from heaters with lower efficiencies (10 percent, for instance) cannot be accurately analyzed using an energy balance because small errors in cooling-water ΔT,

water flow rate, arc power, etc., would cause large errors in the estimates of total enthalpy of the gas flow.

Using the energy-balance technique, air total enthalpy at the STF nozzle throat was calculated as follows:

$$h_{t,1} = \frac{(\dot{m}h)_{arc\ air} + (EI)_{arc} + (\dot{m}h)_{byp\ air} - (\dot{Q}_{UE} + \dot{Q}_{DE} + \dot{Q}_{PR} + \dot{Q}_{PL} + \dot{Q}_{TH})}{\dot{m}_1} \quad (1)$$

where the losses to the individual water-cooled components are computed using

$$\dot{Q} = (\dot{m}c_p\ \Delta T)_{H_2O} \quad (2)$$

This equation assumes steady-state conditions since no heat-storage terms are included. Steady test-flow conditions in the facility were achieved less than one second after arc initiation; however, all runs were at least 10 seconds in length. This permitted heater-component cooling-water ΔT's to reach steady state for use in the energy-balance equation. All other quantities were constant during the test.

The energy content of the supply air and energy added by the electric arc is accounted for as follows:

Losses to the upstream electrode, percent	9.2
Losses to the downstream electrode, percent	29.4
Losses to the plenum rings, percent	0.3
Losses to the plenum chamber, percent	2.0
Losses to the nozzle throat, percent	3.8
Energy in the test air, percent	55.3
Total, percent	100.0

Sonic-throat method.- The sonic-throat technique for determining total enthalpy is discussed in detail in reference 12. Rapidly expanding air approaching the nozzle throat can be in an equilibrium, a frozen, or a non-equilibrium state. Analyses in reference 12 indicate that the heated air in the STF should be in vibrational and chemical equilibrium as it approaches the facility nozzle throat. Therefore, the equilibrium sonic-throat method was used at the conditions in the STF rather than the method for frozen flow.

The pressure-rise sonic-throat technique (ref. 12) was used to estimate throat total enthalpy. Facility air mass flow rate was constant before and during arc-on conditions; therefore, addition of heat to the air was the sole cause of stagnation-pressure rise. Corrections were made for variations in throat discharge coefficient (between arc-on and arc-off conditions) and throat heat loss as discussed in reference 12.

As noted in reference 13, swirl of the air in vortex-stabilized arc heaters can introduce uncertainties in the sonic-throat method by inducing radial pressure gradients in the heater and plenum chamber which complicate the determination of throat discharge coefficient. In the STF, the air that passes through the arc heater is swirled into a chamber between the electrodes. However, the bypass air is injected radially into the flow exiting the heater. With this flow situation, the outer-wall (measured at the beginning of the nozzle) and center-line values (measured at the upstream end of the heater) of $p_{t,1}$ agree within 7 percent or less when room-temperature air flows through the heater before the arc is fired. This indicates that the swirl component is diminished by the radial injection of the bypass flow (the pressure difference from the center line to the wall is much greater if no bypass air is added to the swirled-in arc air). During hot flow (with the electric arc on and the magnetic field energized), the center-line and wall values of pressure normally agree within 1 to 2 percent. It should be noted, however, that for a given mass flow rate, the difference between wall and center-line pressure in a swirling flow is a function of throat size and throat geometry. To minimize any uncertainties due to swirl, average values of center-line and outer-wall pressure were used in the sonic-throat method.

Total-temperature probe.- During a series of arc-heater calibration tests in the STF, a total-temperature probe was mounted in the flow just downstream of a temporary throat. (See fig. 10.) The thermocouple was annealed iridium-iridium/40 percent rhodium which had been calibrated up to 1944 K (3500°R) in a blackbody furnace against a National Bureau of Standards platinum-platinum/13 percent rhodium thermocouple in an argon atmosphere. The probe was designed to minimize velocity, conduction, and radiation losses. (See ref. 14.) Calculations indicated that these losses caused the probe to read about 67 K (120°R) low at a total temperature of 1806 K (3250°R). Corrections for velocity, conduction, and radiation losses were added to the raw thermocouple data which ranged from 1575 to 1936 K (2835° to 3485°R). It must be noted, however, that the radiation correction is subject to error caused by changes in thermocouple emissivity due to plating of copper oxide onto the thermocouple bead. The accuracy of the corrections for velocity losses and heat conduction is also uncertain at these temperature levels. The corrected total temperature, together with measured plenum pressure, was used to estimate total enthalpy.

A comparison of total enthalpy at the throat as determined from the energy-balance measurement, the sonic-throat method, and the total-temperature measurement is shown in figure 11. The energy-balance and sonic-throat methods are in relative agreement, but the thermocouple indicates lower values of enthalpy. The energy-balance technique was the primary method used to determine total enthalpy in this investigation. The method is independent of the kinetic state of the gas and yields accurate results because of the high efficiency of the heater.

Stagnation-point pressure and heating rate.- The total enthalpy in the facility test section is the same as that at the throat if the gas has expanded adiabatically through the nozzle. This assumption is commonly used; however, an attempt to verify it in the STF has been made using nozzle exit pitot pressure and stagnation-point heat-transfer rate. Both measurements were obtained using 7.94-mm (0.313 in.) diameter, flat-faced, cylindrical probes mounted on

rakes. The stagnation-point heating rates were measured using Gardon gauges. (See ref. 11.)

The total enthalpy at the various points where the probes were located was calculated as follows:

$$\dot{q}\sqrt{\frac{r_{eff}}{p_{t,2}}} = 0.0461(h_{t,1} - 130) \tag{3}$$

where r_{eff} is in ft, $\dot{q}$ is in Btu/ft^2-sec, $p_{t,2}$ is in atm, and $h_{t,1}$ is in Btu/lbm. This equation is of the form given in reference 15; however, the effective probe radius was obtained experimentally from calibration tests in a ceramic-heated facility where the total enthalpy of the flow was well established.

A comparison of the point measurements of total enthalpy at the nozzle exit with the bulk enthalpy from the equilibrium sonic-throat method is shown in figure 12. Although the area-weighted average enthalpy determined from the probe measurements is less than the sonic-throat value (as expected, because of boundary-layer heat losses), the flow-core enthalpies are in relatively good agreement. Thus, within the accuracy of both methods, throat values of total enthalpy are valid in the test section.

Nozzle Exit Conditions

For the scramjet-engine test series, hot-flow nozzle exit conditions were obtained by assuming equilibrium flow through the nozzle and using measured pitot pressure, plenum pressure, and throat total enthalpy. The probable existence of nonequilibrium flow through the nozzle is recognized, but effects of chemical nonequilibrium or freezing would be negligible at these test conditions. Freezing of the vibrational modes of the diatomic molecules in the test air is probable, but it would have relatively small effects on the flow parameters. However, since no measurements were obtained which clearly indicated departure from equilibrium, the flow was assumed to be in equilibrium. The exit pitot pressure was measured with a probe mounted beneath the engine, which was in the center of the hot flow when the model was retracted. As is shown in a subsequent section, the pitot profiles at the nozzle exit were relatively uniform.

Other nozzle exit static properties and parameters were calculated using curve fits to equilibrium air nozzle expansion data obtained from a computer program described in reference 16. The average conditions for the scramjet tests are as follows (maximum deviations from the average are shown only for the stagnation conditions):

$$p_{t,1} = 2.89\ ^{+0.22}_{-0.15}\ MN/m^2 \qquad \left(28.5\ ^{+2.2}_{-1.5}\ atm\right)$$

$T_{t,1} = 2180\ ^{+367}_{-243}$ K $\quad \left(3925\ ^{+661}_{-438}\ ^{\circ}R\right)$

$h_{t,1} = 2.51\ ^{+0.50}_{-0.33}$ MJ/kg $\quad \left(1080\ ^{+217}_{-140}\ \text{Btu/lbm}\right)$

$\dot{m}_1 = 2.30$ kg/s $\quad (5.07$ lbm/s)

$M_1 = 6.08$

$p_1 = 1.23$ kN/m^2 $\quad (25.6$ lbf/ft^2)

$T_1 = 297$ K $\quad (535^{\circ}R)$

$\rho_1 = 0.0144$ kg/m^3 $\quad (2.79 \times 10^{-5}$ slug/ft^3)

$V_1 = 2100$ m/s $\quad (6891$ ft/s)

$h_1 = 0.30$ MJ/kg $\quad (128$ Btu/lbm)

$\gamma_1 = 1.4$

$q_1 = 31.7$ KN/m^2 $\quad (663$ lbf/ft^2)

$R_1 = 1.65 \times 10^6$/m $\quad (5.02 \times 10^5$/ft)

These average flow conditions would occur at the scramjet inlet if the engine were mounted on an aircraft flying at the following conditions:

$M_\infty = 6.9$

Altitude = 35.14 km (115 300 ft)

Forebody wedge angle = 4.7°

$q_\infty = 19.3$ kN/m^2 (403 lbf/ft^2)

Test-Flow Uniformity

Pitot-pressure and stagnation-point heating-rate surveys were made in the test cabin to assess the quality of flow which would enter the scramjet engine. Two separate rakes were used for the pitot and heating-rate measurements; each contained 13 probes. All probes were 7.94 mm (0.313 in.) in diameter and were flat-faced cylinders aligned with the flow (flat face normal to flow). The stagnation-point heating rates were measured with Gardon-type gauges. (See ref. 11.)

The surveys were obtained (without the scramjet in the test section) at the facility-nozzle exit and 57.15-cm (22.5-in.) downstream of the nozzle exit. The former survey was used to assess the uniformity of the flow entering the

upstream portion of the scramjet inlet, and the latter survey was used to assess the flow at the beginning of the scramjet cowl.

Because of inadequate regulator control during the survey tests, the nominal value of the unheated peripheral airflow rate was 7.48 kg/s (16.5 lbm/s). This resulted in a higher peripheral-flow nozzle exit static pressure than that of the hot flow; however, the data show the problems associated with nozzle exit pressure mismatching. The majority of the scramjet tests were conducted with reduced peripheral-nozzle airflow rates as discussed subsequently.

The pitot-pressure survey data are shown in figure 13, and the stagnation-point heating-rate surveys are shown in figure 14. At the nozzle exit station, the pitot survey was measured 6.80 cm (2.68 in.) from the vertical center line, and heating rate was measured both on the vertical center line and 6.80 cm (2.68 in.) off the center line. These measurements, which span most of the inlet width and all of the engine height, show a relatively uniform flow entering the inlet.

Both the heating-rate and pitot surveys at the 57.15-cm (22.5-in.) station were measured 6.80 cm (2.68 in.) off the vertical center line (this is representative of the engine internal flow width near the cowl close-off point). Both profiles are distorted at this station by compression waves originating at the nozzle exits.

Figure 15 is a flow schematic, for the test conditions of figures 13 and 14, which shows compression waves measured from schlieren photographs and their locations relative to the scramjet engine. Because of the flow complexity, wave locations were not calculated; instead, the waves from the schlieren photographs were traced to their approximate origins. The source of the wave from the nozzle top surface is the pressure difference between the hot nozzle exit flow and the test-cabin flow. Likewise, pressure differences exist between the hot and unheated flow on the sides and bottom of the hot-flow nozzle as well as between the unheated flow and the test-cabin flow on the sides and bottom of the peripheral nozzle. Therefore, compression waves also approach the engine from the sides of the nozzles (90° to the view shown in fig. 15). The waves from both directions cause the distortion of the profiles at the 57.15-cm (22.5-in.) station. The profiles shown in figures 13 and 14 and the wave schematic shown in figure 15 (where the engine position is shown for illustrative purposes) indicate a potential problem with scramjet tests in this flow if nozzle exit pressures are mismatched, in particular, when the peripheral-nozzle exit pressure is greater than that of the heated flow. Although the wave generated at the top of the facility nozzle would be eliminated by the scramjet (this was verified by scramjet internal pressure distributions), waves from the nozzle bottoms and sides would impinge on the engine ahead of the cowl closure point. The problem of waves interacting with the engine was solved as shown in a subsequent section.

Test-Section/Diffuser Static-Pressure Distributions

Static pressures were measured from the nozzles exits throughout the test section and diffuser. These pressure distributions are shown in figure 16. The top curve was obtained from the same tests as the data shown in figures 13 to 15 without the scramjet in the flow. The other curves in figure 16 were obtained with various peripheral-nozzle airflow rates with the scramjet in the flow. The intent was to assess the effect of peripheral airflow rate on test-cabin and diffuser static pressures so that the wave system at the nozzle exit could be assessed relative to the scramjet model. During these tests, the hot-nozzle airflow rate was held constant at ≈2.30 kg/s (≈5 lbm/s). A peripheral-flow rate of approximately 6.35 kg/s (14 lbm/s) would be required to match the unheated peripheral-flow nozzle exit pressure with the nominal hot-nozzle exit pressure of 1.23 kN/m^2 (0.178 psia). As can be seen from the figure, at that peripheral-flow rate, the test-cabin pressure would be higher than the matched nozzle exit pressures. Therefore, a compression wave would be generated from the juncture of the peripheral flow and the test-cabin flow, and it appears desirable to operate with lower peripheral airflow rates. Wave systems approaching the scramjet are discussed in the next section.

For all of the facility flow rates shown, subsonic flow exists in the diffuser approaching the aftercooler as indicated by the increasing pressure in the diverging area. Diffuser pressure levels generally changed proportionally to the mass flow rate. At the lowest mass flow rate the pressure increased very little between the test section and the 10.67-m (35-ft) station in contrast to the pressure increase at the higher flow rates. A comparison of data with and without a pitot probe attached to the scramjet shows that the additional blockage of the probe caused test-section pressures to increase for a given value of facility air mass flow rate.

FACILITY-MODEL INTERACTION

Description of Interaction

Initial tests of the scramjet were conducted with a peripheral-nozzle airflow rate of 4.08 kg/s (9 lbm/s), that is, with peripheral-nozzle exit pressure less than the hot-nozzle exit pressure. Hot-flow conditions were near the nominal conditions previously stated. Tests without hydrogen fuel indicated that the tunnel and model flows were started and that the scramjet inlet pressures agreed with previous inlet data (ref. 10) obtained in a conventional wind tunnel. (See fig. 17.) Some peak pressures in the strut region shown in the inlet component data were not detected in the engine data because of differences in location of pressure orifices. The agreement between the two sets of inlet pressure data suggested that inlet capture, total-pressure recovery, throat Mach number, etc. from the inlet tests were applicable to the engine tests.

The first tests with hydrogen fuel injection into the scramjet (with subsequent burning) were conducted with the peripheral-nozzle flow conditions stated previously and with the nominal hot-nozzle flow conditions. The test model consisted of the scramjet with a pitot probe mounted beneath the engine (fig. 18). Although the pitot probe and its support rig were designed to be

outside the test flow when the model was in the test position, effects of the probe blockage on test-cabin pressures were noted as pointed out in figure 16. As shown in figure 19(a), injection of a fuel equivalence ratio of 0.65 into the scramjet resulted in increases in the test-cabin pressure, the peripheral-nozzle exit static pressure, and the model drag; that is, a facility-model interaction occurred. Hot-flow nozzle exit pressure was not affected. Model internal inlet pressures (not shown) changed very little from the fuel-off values except for some increases near the cowl. This indicated that the origin of the interaction was external to the scramjet.

With test conditions remaining the same, fuel equivalence ratio was increased to approximately 1.0 on the next test. The facility-model interaction was more pronounced as shown in figure 19(b). Test-cabin pressure and peripheral-nozzle exit static pressure had larger increases than at the lower fuel equivalence ratio, and hot-nozzle exit static pressure also increased with apparent nozzle boundary-layer separation. The scramjet drag increased and the inlet unstarted with large increases in internal inlet pressures.

The cause of the facility-model interaction is believed to be incomplete burning of the hydrogen fuel in the scramjet with subsequent burning downstream in the facility diffuser duct where the hot-engine flow, the hot-nozzle flow, and the unheated peripheral-nozzle flow mixed. Motion pictures confirmed that burning occurred in this region since impurities in the air made the hydrogen flame visible. The tunnel diffuser could not maintain fuel-off test-cabin pressure levels with this downstream combustion.

With the aid of figure 20, the facility-model interaction is explained as follows: Consider a case where both hot-nozzle and peripheral-nozzle air mass flow rates remain constant while fuel flow is gradually increased (in the example shown, $\dot{m}_{\eta} = 2.30$ kg/s (5 lbm/s) and $\dot{m}_{ph} = 4.08$ kg/s (9 lbm/s)). Figure 20 shows the wave structure at the nozzle exits before hydrogen fuel is injected into the scramjet. Expansion waves from the hot-flow and peripheral-flow junctures sweep across the cowl forward-facing surfaces. However, a weak shock also sweeps this surface. As the test-cabin pressure increases with increasing fuel flow rate, the shock wave from the juncture of the peripheral-flow nozzle and the cabin becomes stronger, and its intersection point on the scramjet moves upstream and encompasses more of the cowl forward-facing surface. Waves striking this surface are responsible for the increases in scramjet drag when fuel is injected. At cabin pressures below those necessary to unstart the peripheral-nozzle flow, this shock wave is turned away from the model (as in the case shown in fig. 20) when it intersects the slipstream emanating from the juncture of the hot and unheated flows. This shock will be further weakened if it intersects the expansion wave in the hot flow. (This argument is partially qualitative because of the extremely complicated nozzle exit flow, which includes mixing between heated and unheated flows as well as shock waves, expansion waves, and slipstreams, all intersected at 90° by similar waves from the sides of the nozzle.)

As more fuel is injected and the cabin pressure rises above the value required to separate the peripheral-nozzle boundary layer (ref. 17), the situation relative to the model changes drastically. Shocks form upstream in the peripheral-flow nozzle and, in addition, the static pressure at the peripheral-

nozzle exit exceeds the static pressure at the exit of the hot-flow nozzle. Then a shock wave in the hot flow emanates towards the model (i.e., when $p_{ph} > p_1$). At still higher cabin pressures, this shock wave intersects the inlet upstream of the cowl closure point and, eventually, both the hot-nozzle flow and the inlet flow unstart.

Effects of Nozzle Extensions

The first attempt to remedy the facility-model interaction problem consisted of adding nozzle extensions to both the hot-flow and peripheral-flow nozzle exits as shown in figures 3, 21(a), and 21(b). (To decrease flow blockage, the pitot probe mounted beneath the model was removed.) The extensions were designed to extend the beginnings of the nozzle exit compression (or expansion) waves downstream, preventing wave impingement on cowl forward-facing surfaces and possible entry into the scramjet inlet.

The extensions were successful, at the lower values of fuel equivalence ratio, in decreasing the amount of facility-model interaction. This is evident in figure 22, where cabin pressure, peripheral-flow nozzle exit pressure, and scramjet drag are compared for a fuel equivalence ratio of 0.65 with and without nozzle extensions (peripheral-airflow rate was 4.08 kg/s (9 lbm/s) in both cases; therefore, $\frac{p_{ph}}{p_1} < 1$ since the match point would occur at $\dot{m}_{ph}$ = 6.35 kg/s (14 lbm/s)). Note that with extensions, the peripheral-nozzle pressure (which was now measured further upstream because of the extended nozzle exit) was not affected when fuel was injected, even though test-cabin pressure did increase. This indicates that the disturbance in this nozzle was moved downstream by the extension on the peripheral-flow nozzle. Negligible increases in scramjet drag were noted with this level of fuel injection; however, at higher fuel equivalence ratios, facility-model interaction did occur again and scramjet drag was increased. Drag increases at a given fuel equivalence ratio were always less with the nozzle extensions than without the extensions. It should also be noted that zero-fuel drag was less with the extensions (fig. 22(b)) than without them (fig. 22(a)). With the extensions added to the nozzles and with the pitot probe removed, scramjet inlet unstart could not be made to occur, even for injected fuel equivalence ratios as high as 1.2; however, without the extensions and with the pitot probe installed, unstart occurred at fuel equivalence ratios of about 1.

Engine internal pressures and heating rates showed little evidence of burning inside the scramjet. This lack of internal combustion perhaps contributed to tne facility-model interaction problem (because the fuel burned downstream in the facility diffuser). However, the course of action at this point in the test program was to solve the interaction problem without making internal scramjet geometry changes to enhance combustion in the scramjet.

Effects of Decreasing Peripheral-Airflow Rate

Since the addition of nozzle extensions was only partially successful in alleviating the facility-model interaction problem, efforts turned to finding a method of eliminating, or minimizing, the test-cabin pressure rise associated with hydrogen fuel injection into the scramjet. This could be accomplished with a modification designed to make the facility diffuser more efficient. The same effect, however, was achieved by reducing the total mass flow rate passing through the tunnel diffuser, that is, by reducing the peripheral-airflow rate. Peripheral-nozzle airflow was varied over a series of tests with values of 4.08, 2.72, and 0.59 kg/s (9, 6, and 1.3 lbm/s). Measured test-section and diffuser pressures for these peripheral-nozzle airflow rates with no hydrogen fuel injection are shown in figure 16, where the heated air mass flow rate was nominally 2.30 kg/s (5 lbm/s).

Test-section and diffuser pressures with hydrogen fuel injection for these same peripheral-nozzle airflow rates (with the exception of the 7.48 kg/s (16.5 lbm/s) peripheral-flow rate) are shown in figure 23. The zero-fuel pressure distributions from figure 16 are also plotted and connected by the solid lines. The injection of hydrogen fuel increases the level of the test-section/diffuser pressure distributions at most stations for all three peripheral-nozzle airflow rates. However, the test-cabin pressure is affected more by a given increase in fuel-injection rate at the higher peripheral-nozzle airflow rates than at the lower airflow rates. In addition, the test-cabin pressure is always less than the nominal hot-flow nozzle exit static pressure regardless of the amount of fuel injected at the lowest peripheral-airflow rate of 0.59 kg/s (1.3 lbm/s).

The pressure at the 10.67-m (35-ft) station is always significantly higher than test-section pressure (even without fuel injection) except for the 0.59-kg/s (1.3-lbm/s) case. At the highest fuel equivalence ratio, the pressure at this station did show a large increase for the low peripheral-flow case, perhaps indicating burning farther upstream in the diffuser duct. The data (figs. 16 and 23) indicate that the pressure at the 10.67-m (35-ft) station is sensitive to both fuel equivalence ratio and flow blockage.

The effect on test-cabin pressure and scramjet drag caused by a change in airflow rate at a fixed value of fuel equivalence ratio is illustrated in figure 24. In this test, the peripheral-flow rate was initially 4.08 kg/s (9 lbm/s). No nozzle extensions were used, and no pitot probe was mounted beneath the scramjet. Test-cabin pressure was 1.59 kN/m^2 (0.230 psia), and scramjet drag was 284 N (64 lbf) prior to fuel injection. When fuel was injected into the scramjet at an equivalence ratio of ≈1.05, interaction occurred with cabin pressure increasing to 2.90 kN/m^2 (0.420 psia) and scramjet drag increasing to 383 N (86 lbf). Next, peripheral-airflow rate was reduced to zero with the fuel-injection rate of 1.05 times the stoichiometric rate maintained. Note the immediate drop in cabin pressure, which eventually reaches 0.14 kN/m^2 (0.020 psia). Scramjet drag decreased to 200 N (45 lbf). After fuel injection was terminated, scramjet drag increased very little, indicating poor combustion of the hydrogen fuel in the scramjet.

The dependence of test-cabin pressure on peripheral-nozzle air mass flow rate and on fuel equivalence ratio is shown in figure 25. Open symbols are data obtained with no pitot probe in the flow, and shaded symbols are data obtained with a pitot probe in the flow. The nominal hot-flow and peripheral-flow nozzle exit static pressures are shown for reference.

Test-cabin pressure, at a given value of peripheral-flow rate, is always greater than peripheral-flow nozzle exit pressure. Therefore, a shock wave always emanates towards the model from the peripheral-flow/cabin-flow juncture. With a pitot probe attached to the scramjet, test-cabin pressure increases to the point at which separation of the peripheral-flow boundary layer is possible (ref. 17) when $\dot{m}_{ph}$ = 4.08 kg/s (9 lbm/s) and $\dot{m}_t$ = 6.35 kg/s (14 lbm/s) when ϕ_{inj} = 0. Note that cabin pressures are always greater when the pitot probe is in the flow, indicating a sensitivity of the total flow process to total pressure losses.

Test-cabin pressure, at a given value of peripheral-flow rate, increases as the amount of injected fuel is increased. Therefore, peripheral-flow boundary-layer separation certainly occurs at the higher facility mass flow rates and becomes more likely to occur at lower peripheral-flow rates as fuel equivalence ratio is increased. When flow separation occurs in the peripheral-flow nozzle, the peripheral-flow nozzle exit pressure ranges somewhere between the unseparated flow pressure and the test-cabin pressure. As can be seen from figure 25, at the higher peripheral-flow rates with large amounts of fuel injection, it is conceivable that the hot-nozzle flow would become separated. Even if hot-nozzle flow separation did not occur, a shock would certainly exist in the hot flow which, if strong enough, would cause facility-model interaction.

Figure 25 also shows that, even at the high injected fuel equivalence rates test-cabin pressure does not exceed the hot-nozzle exit static pressure at the lowest value of peripheral-flow rate tested, that is, 0.59 kg/s (1.3 lbm/s) where $\dot{m}_t$ = 2.86 kg/s (6.3 lbm/s). Thus, if test-cabin pressure were to cause the peripheral-nozzle flow to separate, hot-flow nozzle exit pressure would still be greater than peripheral-flow nozzle exit pressure. Therefore, no shock waves would exist in the hot flow from the juncture of these two flows. Rather, an expansion fan in the hot flow would be directed towards the scramjet.

Therefore, to eliminate the facility-model interaction, the best facility test mode appears to be low peripheral-nozzle flow 0.59 kg/s (1.3 lbm/s), nozzle extensions added to both nozzle exits, and minimum flow blockage. The extensions assure that no waves, including expansion waves from the hot/unheated flow juncture, affect scramjet drag.

As shown in figure 26(a), fuel-off drag at the lowest peripheral flows shows a slight decrease without nozzle extensions, perhaps because of the hot-flow expansion fan impinging on the scramjet cowl forward-facing surfaces. This same plot shows fuel-off drag increases at the higher peripheral flows with no nozzle extensions, especially with the pitot probe in the flow. These increases are most likely caused by shock waves impinging on the cowl forward-facing surfaces. Fuel-off drag data over the whole range of peripheral-flow rate are relatively constant with the nozzle extensions installed (fig. 26(b)).

Figure 27 is a summary plot which illustrates the history of the elimination of the facility-model interaction. The change in engine force from fuel-off to fuel-on conditions ΔF is plotted against ϕ_{inj}. The theoretical prediction is a goal which assumes mixing-controlled reaction with all-perpendicular fuel injection and 100-percent combustion efficiency. Curve 1 is from data obtained without nozzle extensions, with the pitot probe mounted beneath the scramjet, and with a relatively high peripheral-nozzle airflow rate, 4.08 kg/s (9 lbm/s). (No inlet unstart data are shown.) Facility-model interaction is severe. Curve 2 is from data obtained at the high peripheral-flow rate but with nozzle extensions and without the scramjet pitot probe. Facility-model interaction is decreased but is still present. Curve 3 shows the elimination of the facility-model interaction and is from the first data showing reduction of scramjet drag when fuel was injected. These data were obtained with nozzle extensions, no pitot probe, and a low peripheral-nozzle flow rate of 0.59 kg/s (1.3 lbm/s). Thus, the interaction problem has been overcome. However, engine performance is low because of poor combustion of the fuel in the scramjet. The engine performance remained low during these initial scramjet tests while emphasis was placed on solving the facility-model interaction problem. Tests are now in progress to improve combustion in the scramjet.

CONCLUSIONS

A facility for testing airframe-integrated scramjets differs from conventional aerodynamic facilities in several ways. First, in order to adequately perform tests with combustion, actual flight Mach number total enthalpy has to be duplicated and a reasonable flight altitude must be simulated. Second, simulation of the integration of a flight engine with the vehicle undersurface must be accomplished by testing in a stream with a total enthalpy duplicating flight total enthalpy but with an inlet Mach number which duplicates the Mach number along the vehicle undersurface. Also, the engine inlet should ingest a portion of the facility nozzle boundary layer to simulate the flight situation. The following conclusions were reached using data obtained from facility calibration tests and initial scramjet engine tests in the Langley Mach 7 Scramjet Test Facility:

1. A facility has been developed which is capable of providing simulation of Mach 7 flight conditions for tests of the airframe-integrated scramjet engine.

2. The high total enthalpy of the airflow corresponding to Mach 7 flight conditions is difficult to measure. Throat enthalpies as determined by the sonic-throat method and by an energy-balance technique were in good agreement. However, total enthalpy determined from a total-temperature probe was less than that from the other methods and is more suspect because of corrections required to the thermocouple data.

3. In the Langley Scramjet Test Facility, nozzle exit total enthalpy determined from pitot pressure and stagnation-point heating rates was in agreement with throat total enthalpy determined by the sonic-throat method.

4. At the nominal test condition during the scramjet engine tests, conditions in the facility were such that flight at a Mach number of 6.9 and an altitude of 35.14 km (115 300 ft) was simulated. This corresponds to a flight dynamic pressure of 19.3 kN/m^2 (403 lbf/ft^2). Conditions at the scramjet inlet were representative of a 4.7° vehicle forebody wedge angle.

5. Flow entering the scramjet inlet was relatively uniform over the width and height of the inlet.

6. For the test setup used, flow uniformity at the cowl closure point on the scramjet was a critical function of the tailoring of the nozzle exit flows of the heated test flow and an unheated peripheral flow, that is, matching the nozzle exit pressures.

7. The facility-model interaction was eliminated by adding extensions to the nozzle exits and decreasing the peripheral-nozzle airflow rate to an experimentally determined acceptable level.

Langley Research Center
National Aeronautics and Space Administration
Hampton, VA 23665
January 27, 1981

REFERENCES

1. Henry, John R.; and Anderson, Griffin Y.: Design Considerations for the Airframe-Integrated Scramjet. NASA TM X-2895, 1973.

2. Jones, Robert A.; and Huber, Paul W.: Airframe-Integrated Propulsion System for Hypersonic Cruise Vehicles. ICAS Proceedings 1978 - 11th Congress of the International Council of the Aeronautical Sciences (ICAS), Volume 1 - Fuel Conservation, Hypersonic Vehicles, Environmental Effects, Materials and Structures, Computational Aerodynamics, Wind Tunnels, Flight Testing, Stability and Control, J. Singer and R. Staufenbiel, eds., Sept. 1978, pp. 130-136.

3. Wieting, Allan R.; and Guy, Robert W.: Thermal-Structural Design/Analysis of an Airframe-Integrated Hydrogen-Cooled Scramjet. J. Aircr., vol. 13, no. 3, Mar. 1976, pp. 192-197.

4. Killackey, J. J.; Katinszky, E. A.; Tepper, S.; Vuigner, A. A.; Wright, C. C.; and Stockwell, G. G.: Thermal-Structural Design Study of an Airframe-Integrated Scramjet - Final Report. NASA CR-159039, 1980.

5. Guy, Robert W.; Mueller, James N.; Pinckney, Shimer Z.; and Lee, Louise P.: Thermal Design and Analysis of a Hydrogen-Burning Wind Tunnel Model of an Airframe-Integrated Scramjet. NASA TM X-73931, 1977.

6. Guy, Robert W.; and Mackley, Ernest A.: Initial Wind Tunnel Tests at Mach 4 and 7 of a Hydrogen-Burning, Airframe-Integrated Scramjet. NASA paper presented at the 4th International Symposium on Air Breathing Engines. (Lake Buena Vista, Fla.), Apr. 1-6, 1979.

7. Boatright, William B.; Sabol, Alexander P.; Sebacher, Daniel I.; Pinckney, Shimer Z.; and Guy, Robert W.: Langley Facility for Tests at Mach 7 of Subscale, Hydrogen-Burning, Airframe-Integratable, Scramjet Models. AIAA Paper No. 76-11, Jan. 1976.

8. Smith, Richard T.; and Folck, James L.: Operating Characteristics of a Multi-Megawatt Arc Heater Used With the Air Force Flight Dynamics Laboratory 50-Megawatt Facility. AFFDL-TR-69-6, U.S. Air Force, Apr. 1969.

9. Anders, John B.; Sebacher, Daniel I.; and Boatright, William B.: Fluid Flow Analysis of a Hot-Core Hypersonic-Wind-Tunnel Nozzle Concept. NASA TN D-6768, 1972.

10. Trexler, Carl A.; and Souders, Sue W.: Design and Performance at a Local Mach Number of 6 of an Inlet for an Integrated Scramjet Concept. NASA TN D-7944, 1975.

11. Gardon, Robert: An Instrument for the Direct Measurement of Intense Thermal Radiation. Rev. Sci. Instr., vol. 24, no. 5, May 1953, pp. 366-370.

12. Winovich, Warren: On the Equilibrium Sonic-Flow Method for Evaluating Electric-Arc Air-Heater Performance. NASA TN D-2132, 1964.

13. Folck, James L.; and Smith, Richard T.: Hypersonic Flow Diagnostic Studies in a Large Arc-Heated Wind Tunnel. AIAA J., vol. 8, no. 8, Aug. 1970, pp. 1470-1476.

14. Moffat, Robert J.: Gas Temperature Measurement. Temperature - Its Measurement and Control in Science and Industry, Volume 3, Pt. 2, Reinhold Pub. Corp., c.1962, pp. 553-571.

15. Zoby, Ernest V.: Empirical Stagnation-Point Heat-Transfer Relation in Several Gas Mixtures at High Enthalpy Levels. NASA TN D-4799, 1968.

16. Lordi, J. A.; Mates, R. E.; and Moselle, J. R.: Computer Program for the Numerical Solution of Nonequilibrium Expansions of Reacting Gas Mixtures. NASA CR-472, 1966.

17. Moore, John A.: Investigation of the Effect of Short Fixed Dif[illegible]s on Starting Blowdown Jets in the Mach Number Range From 2.7 to 4.[illegible] NACA TN 3545, 1956.

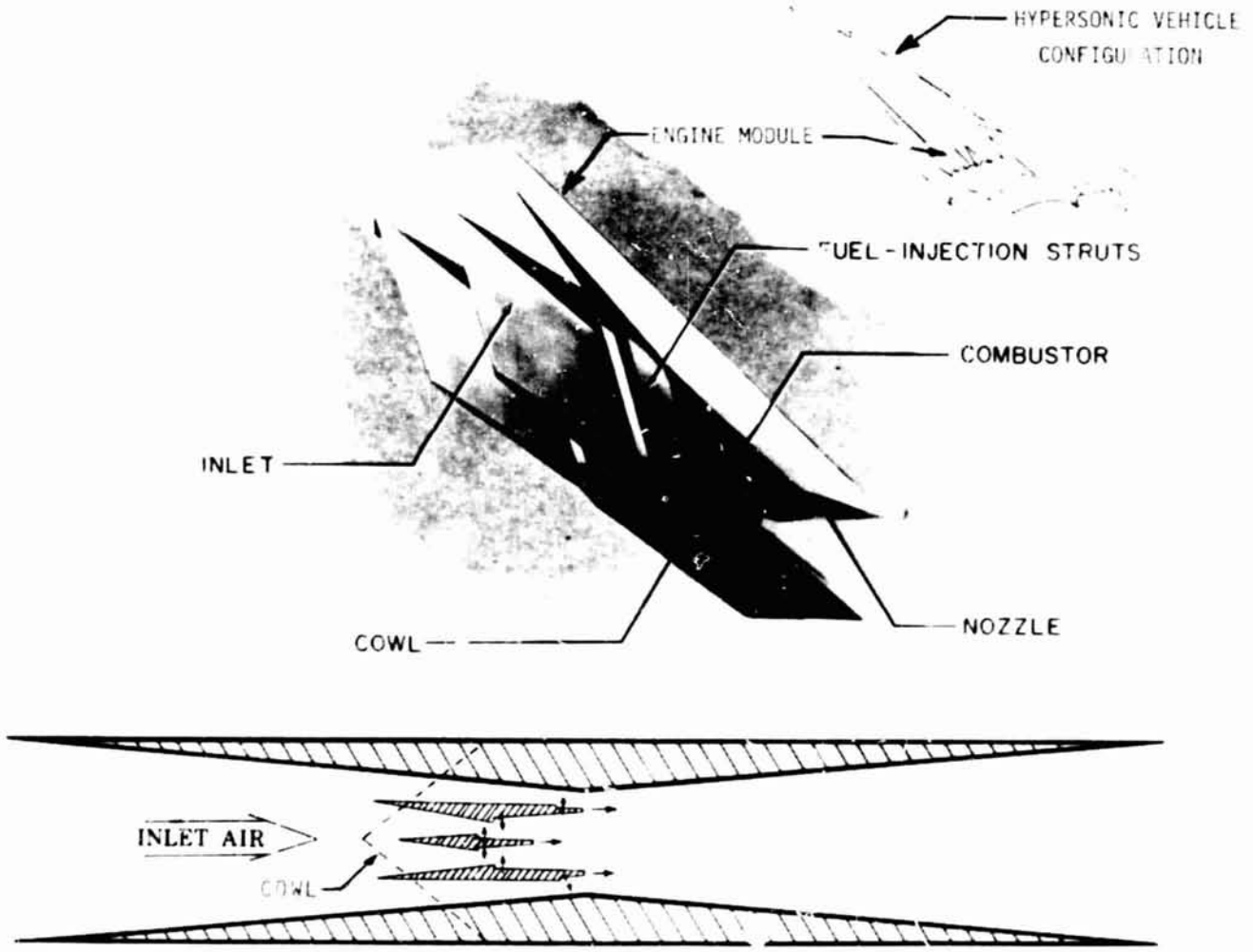

L-81-102

Figure 1.- Airframe-integrated supersonic combustion ramjet.

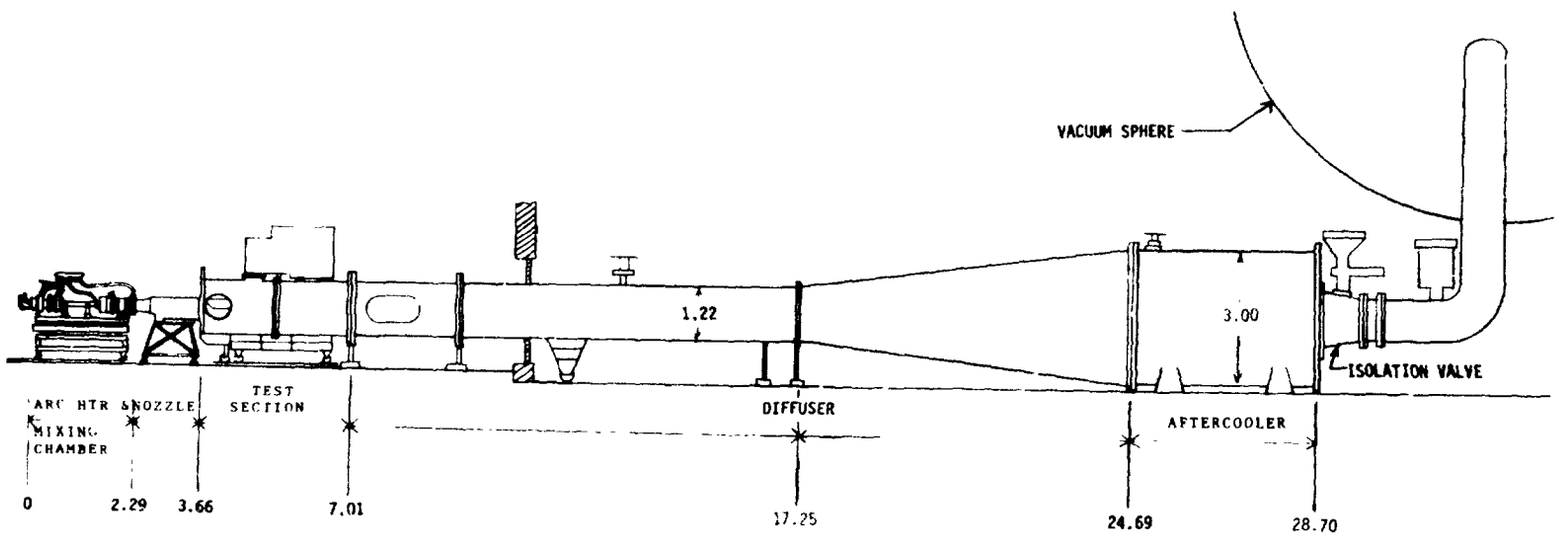

Figure 2.- Elevation view of Langley Mach 7 Scramjet Test Facility. Dimensions are in meters.

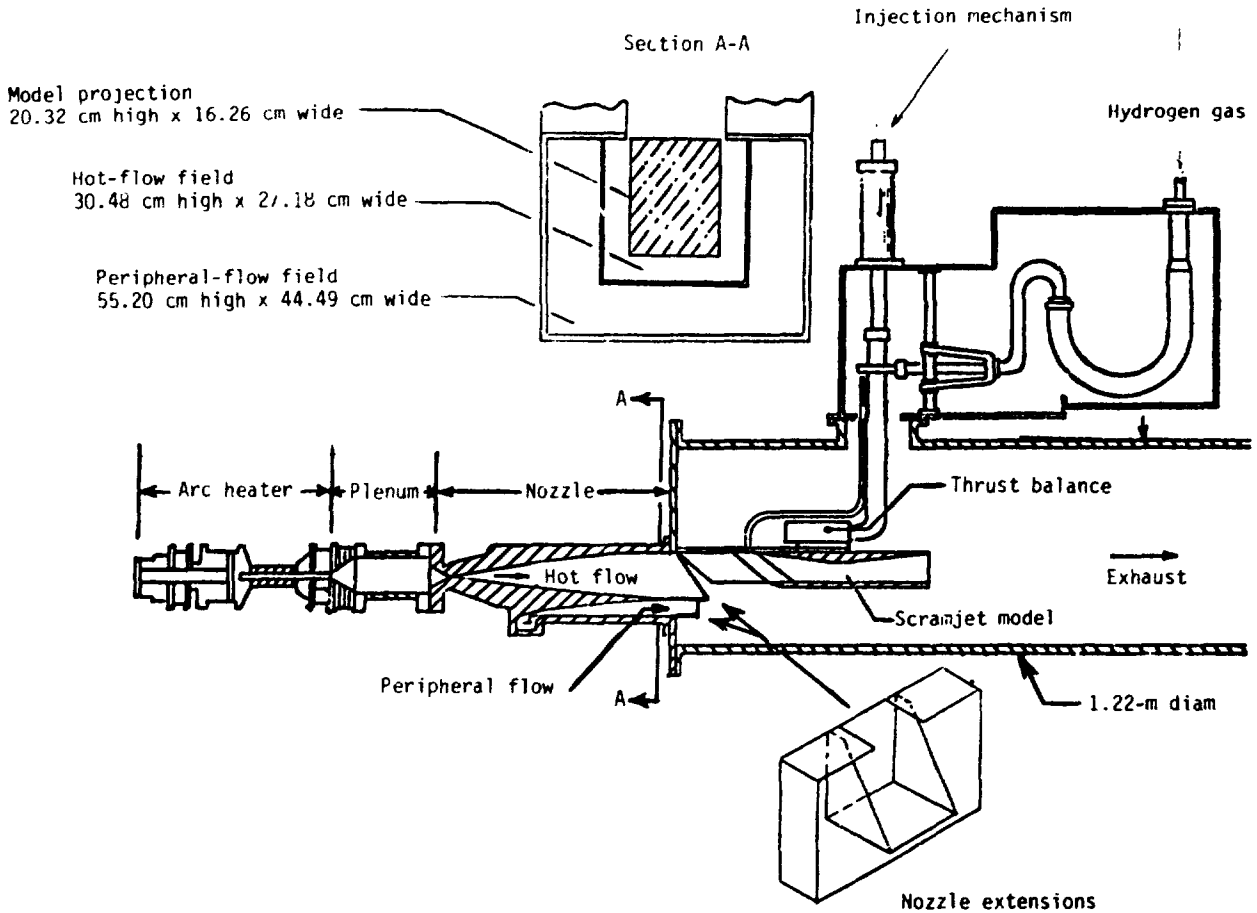

Figure 3.- Test arrangement in Langley Mach 7 Scramjet Test Facility.

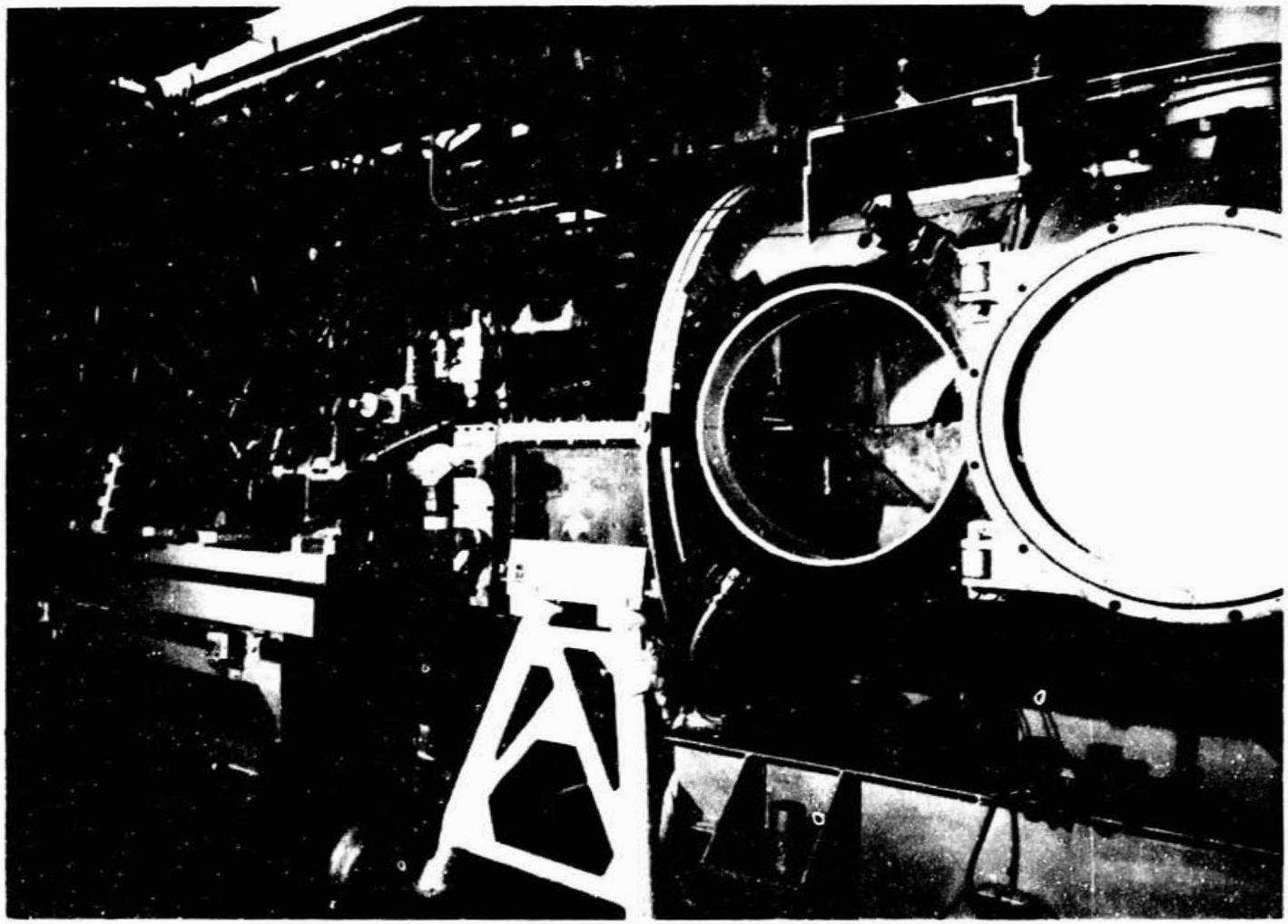

L-77-1593

Figure 4.- Copper engine in Langley Mach 7 Scramjet Test Facility.

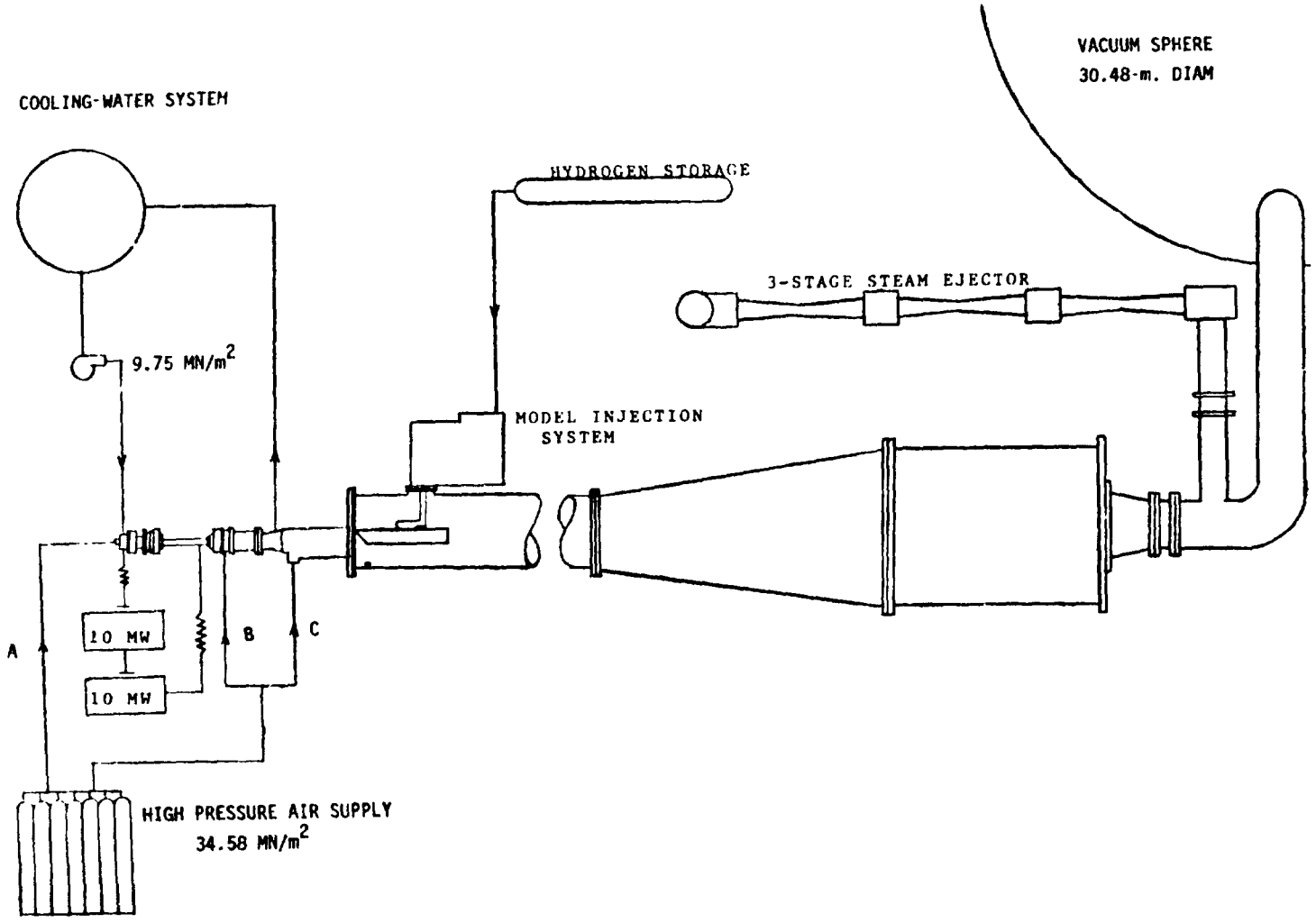

Figure 5.- Major test-facility support systems.

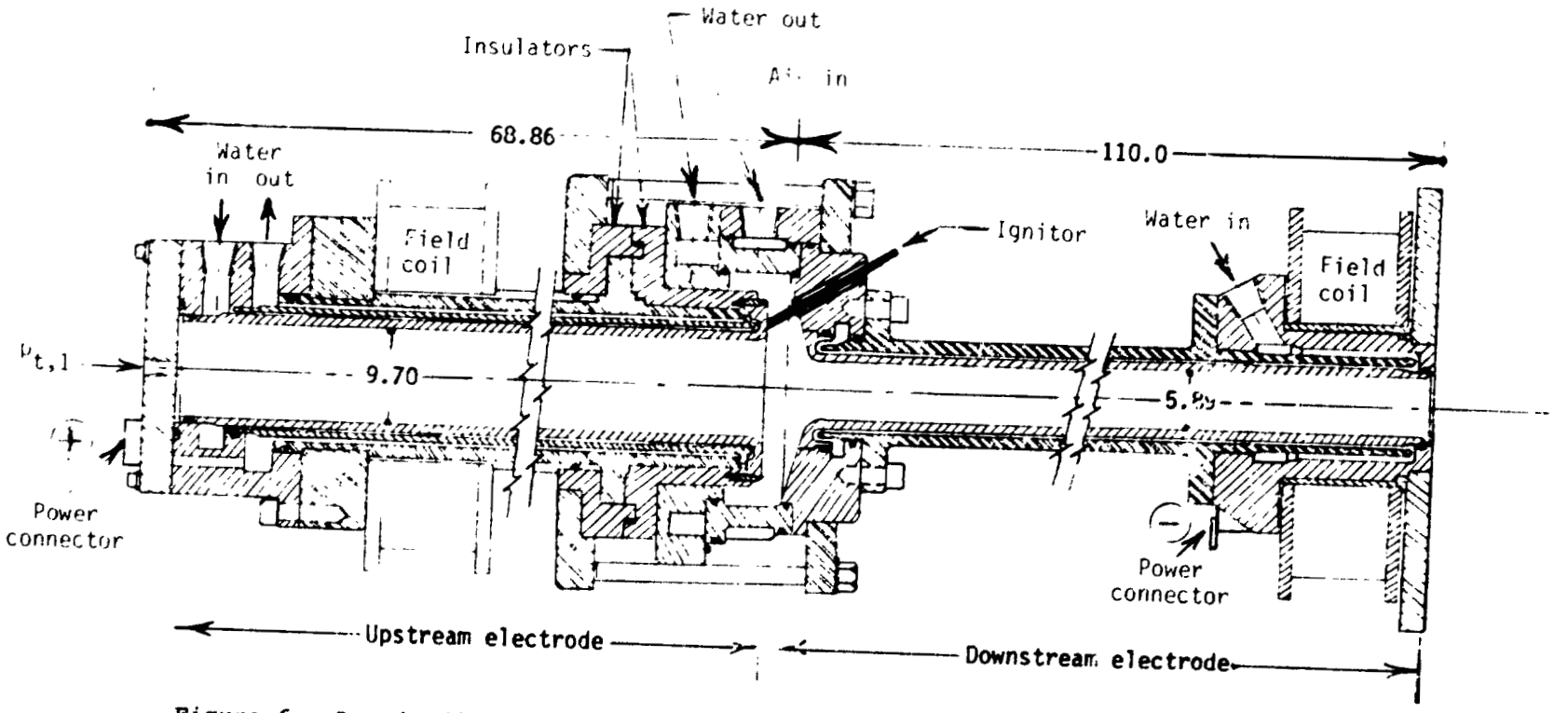

Figure 6.- Longitudinal section view of vortex-stabilized arc heater. Dimensions are in centimeters.

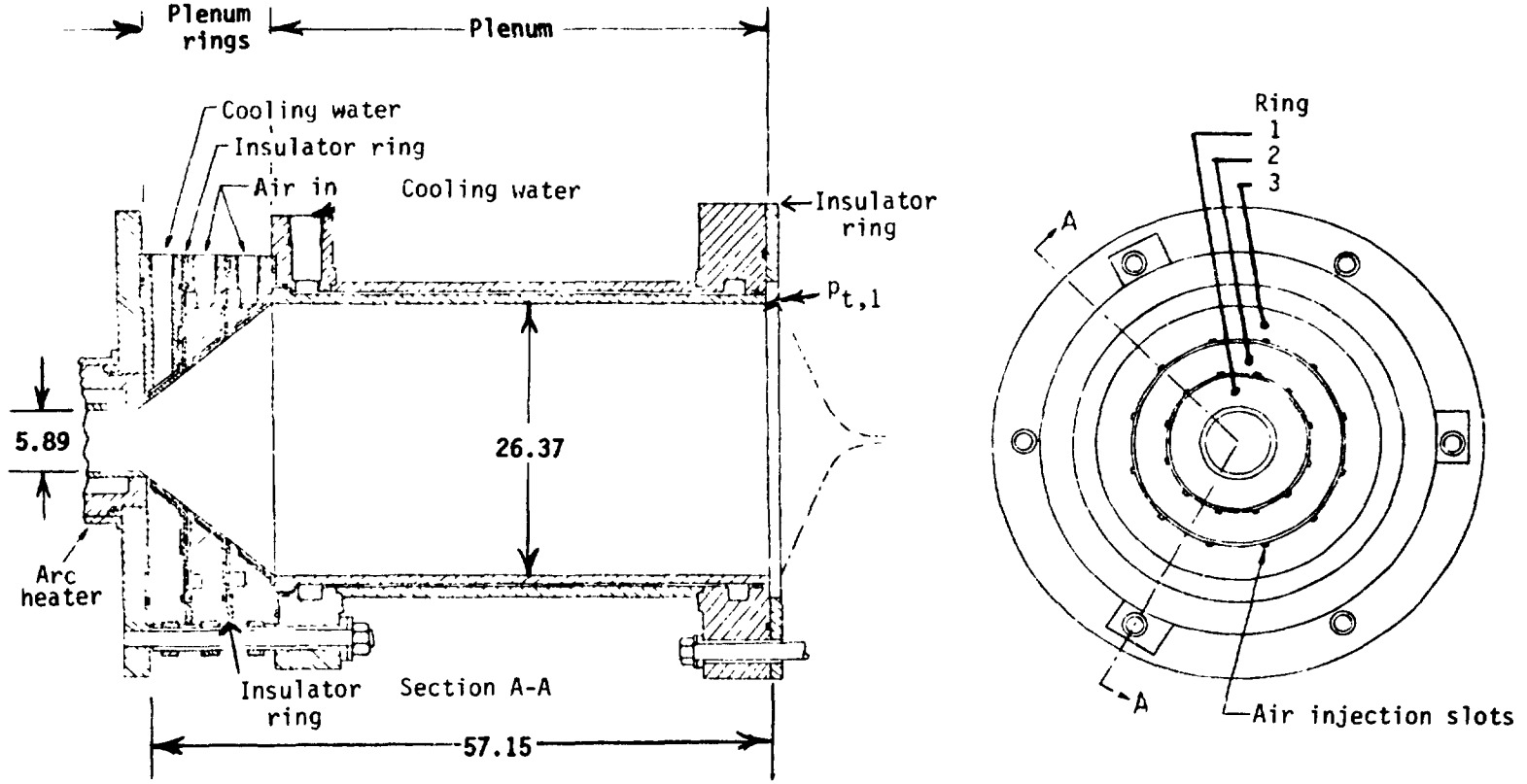

Figure 7.- Sectional view of bypass air-injection slots and plenum chamber. Dimensions are in centimeters.

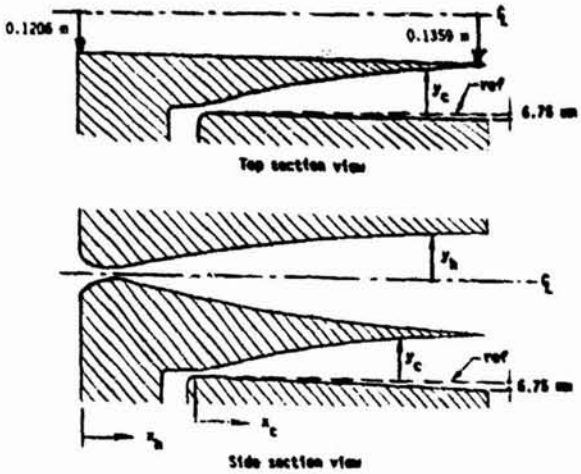

2-D Hot-Flow Nozzle

x_h meters	y_h meters	x_h meters	y_h meters	x_h meters	y_h meters	x_h meters	y_h meters
0	.05080	.05486	.00516	.20625	.02436	.54661	.08933
.00360	.04433	.05852	.00424	.22149	.02786	.57201	.09274
.00610	.03947	.06096	.00356	.23673	.03137	.59995	.09614
.00853	.03597	.06462	.00299	.25197	.03487	.62535	.09919
.00975	.03432	.06828	.00241	.26213	.03721	.67615	.10498
.01219	.03139	.07315	.00192	.27737	.04064	.70155	.10775
.01463	.02873	.07534	.00183	.29261	.04407	.72695	.11046
.01707	.02626	.07925	.00178	.30785	.04747	.76505	.11440
.01951	.02395	.08324	.00182	.32309	.05083	.80315	.11791
.02195	.02184	.08717	.00192	.33833	.05410	.84125	.12106
.02438	.01991	.09360	.00220	.35357	.05723	.87935	.12410
.02682	.01814	.09769	.00246	.36881	.06020	.91745	.12697
.03170	.01496	.10678	.00323	.38405	.06312	.96825	.13058
.03414	.01356	.11740	.00457	.39929	.06594	1.01905	.13378
.03658	.01224	.12819	.00645	.41961	.06947	1.06985	.13663
.04023	.01049	.14021	.00899	.43993	.07290	1.12065	.13924
.04267	.00942	.14580	.01031	.46025	.07620	1.17145	.14173
.04511	.00847	.15545	.01250	.48565	.08016	1.24765	.14501
.04755	.00762	.17577	.01722	.50597	.08331	1.32385	.14747
.05121	.00627	.18131	.02081	.52629	.08639	1.40005	.14958
						1.47625	.15136
						1.54229	.15240

Peripheral-Flow Nozzle

x_c meters	y_c meters	x_c meters	y_c meters	x_c meters	y_c meters	x_c meters	y_c meters
0	.01184	.09652	.02253	.23368	.05822	.50800	.10622
.00508	.01189	.10160	.02370	.24384	.06071	.53340	.10902
.01016	.01196	.10668	.02494	.25400	.06314	.55880	.11168
.01524	.01217	.11176	.02619	.26416	.06551	.58420	.11415
.02032	.01240	.11684	.02738	.27432	.06779	.60960	.11641
.02540	.01265	.12192	.02868	.28448	.07000	.63500	.11854
.03048	.01295	.12700	.02990	.29464	.07214	.66040	.12047
.03556	.01331	.13208	.03122	.30480	.07432	.68580	.12235
.04064	.01369	.13716	.03249	.31496	.07638	.71120	.12395
.04572	.01420	.14224	.03378	.32512	.07838	.73660	.12543
.05080	.01471	.14732	.03513	.33528	.08029	.76200	.12682
.05588	.01527	.15240	.03642	.34544	.08217	.78740	.12804
.06096	.01598	.16256	.03917	.35560	.08395	.81280	.12911
.06604	.01674	.17272	.04194	.36576	.08570	.83820	.13005
.07112	.01755	.18288	.04470	.37592	.08743	.86360	.13094
.07620	.01839	.19304	.04750	.38100	.08829	.88900	.13170
.08128	.01928	.20320	.05027	.40640	.09238	.91440	.13233
.08636	.02029	.21336	.05304	.43180	.09616	.93980	.13283
.09144	.02136	.22352	.05565	.45720	.09975	.96520	.13315
				.48260	.10312	.98806	.13335

Figure 8.- Schematic of hot-flow and peripheral-flow nozzles with coordinates.

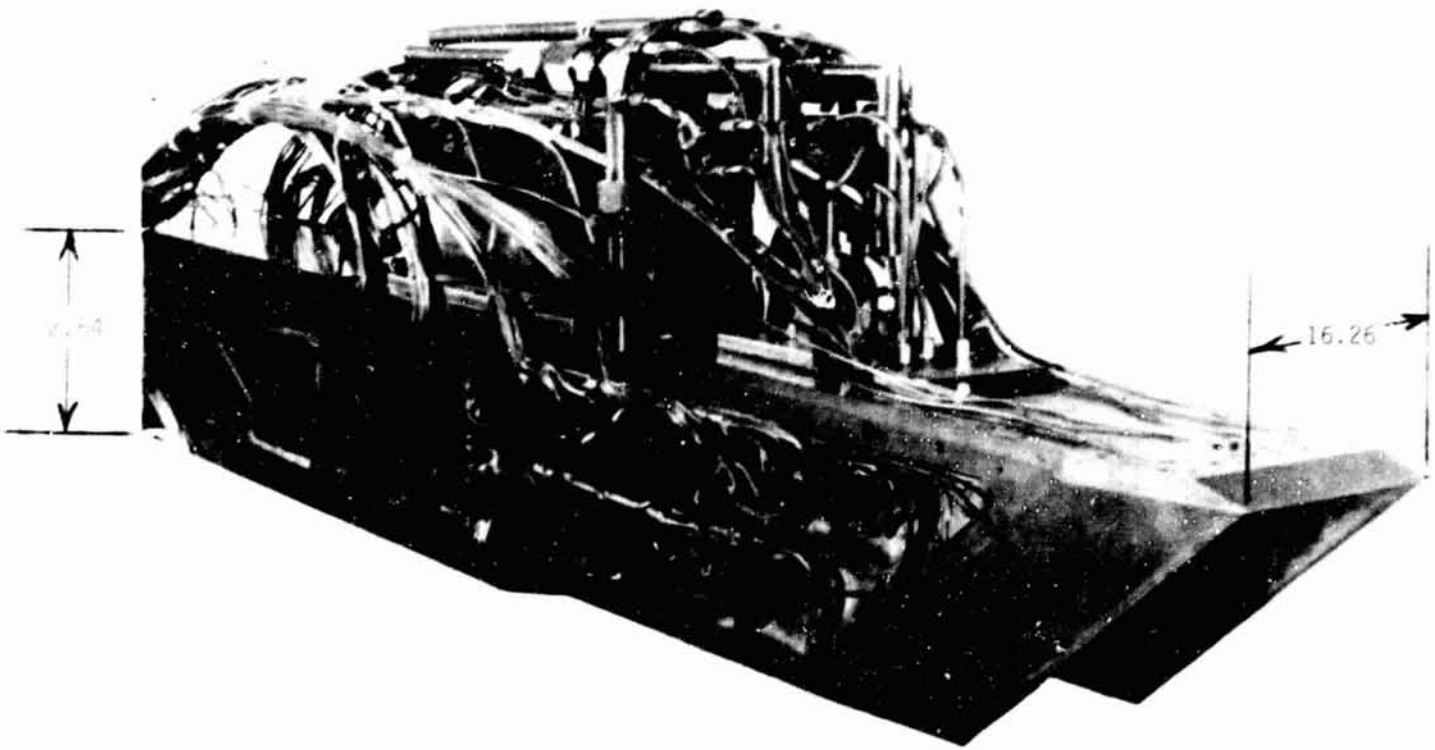

L-80-2036

(a) View of complete engine. Dimensions are in centimeters.

Figure 9.- Copper scramjet engine model.

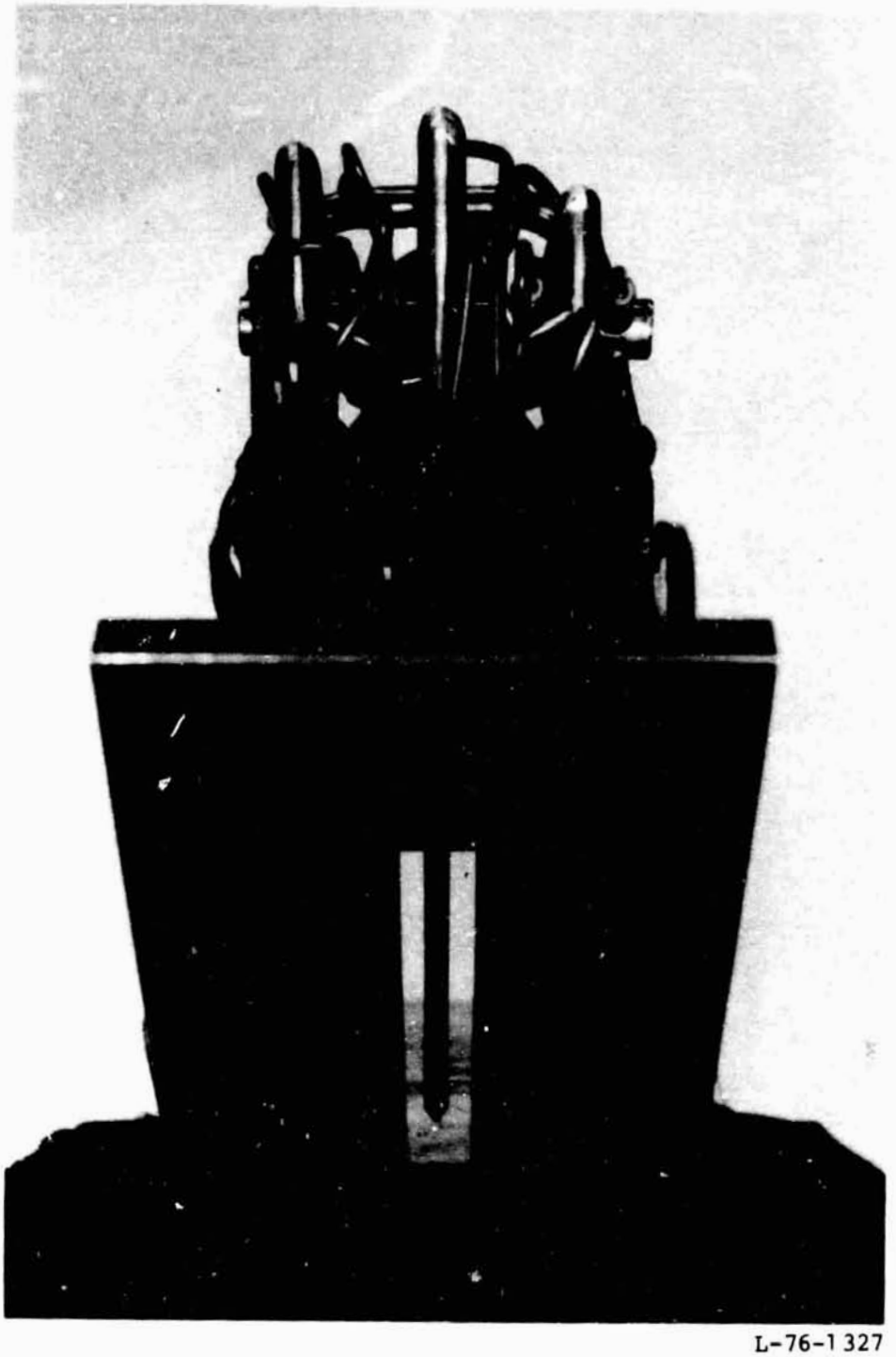

L-76-1327

(b) Front view showing fuel-injection struts.

Figure 9.- Concluded.

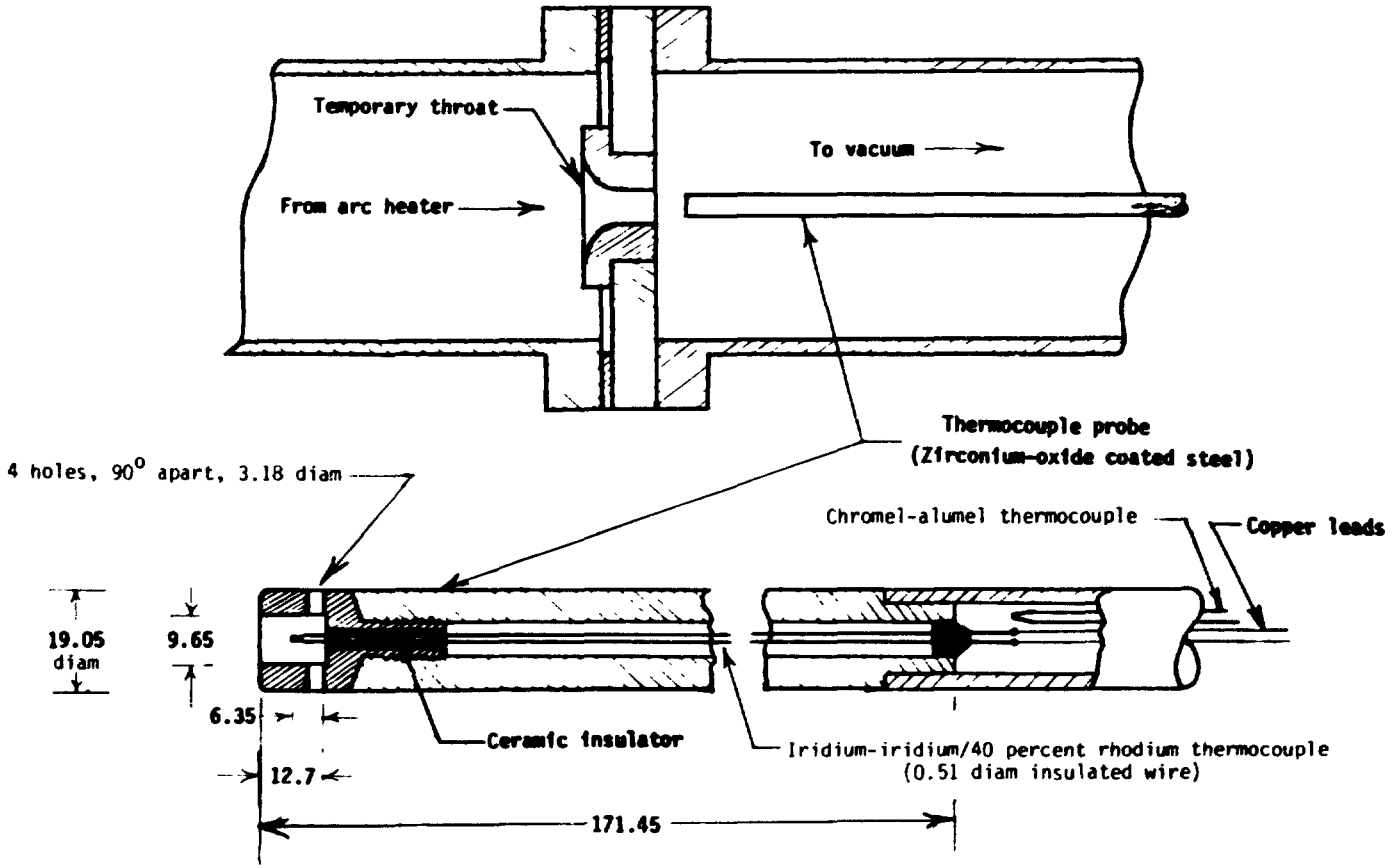

Figure 10.- Detail of total-temperature probe and test arrangement. Dimensions are in millimeters.

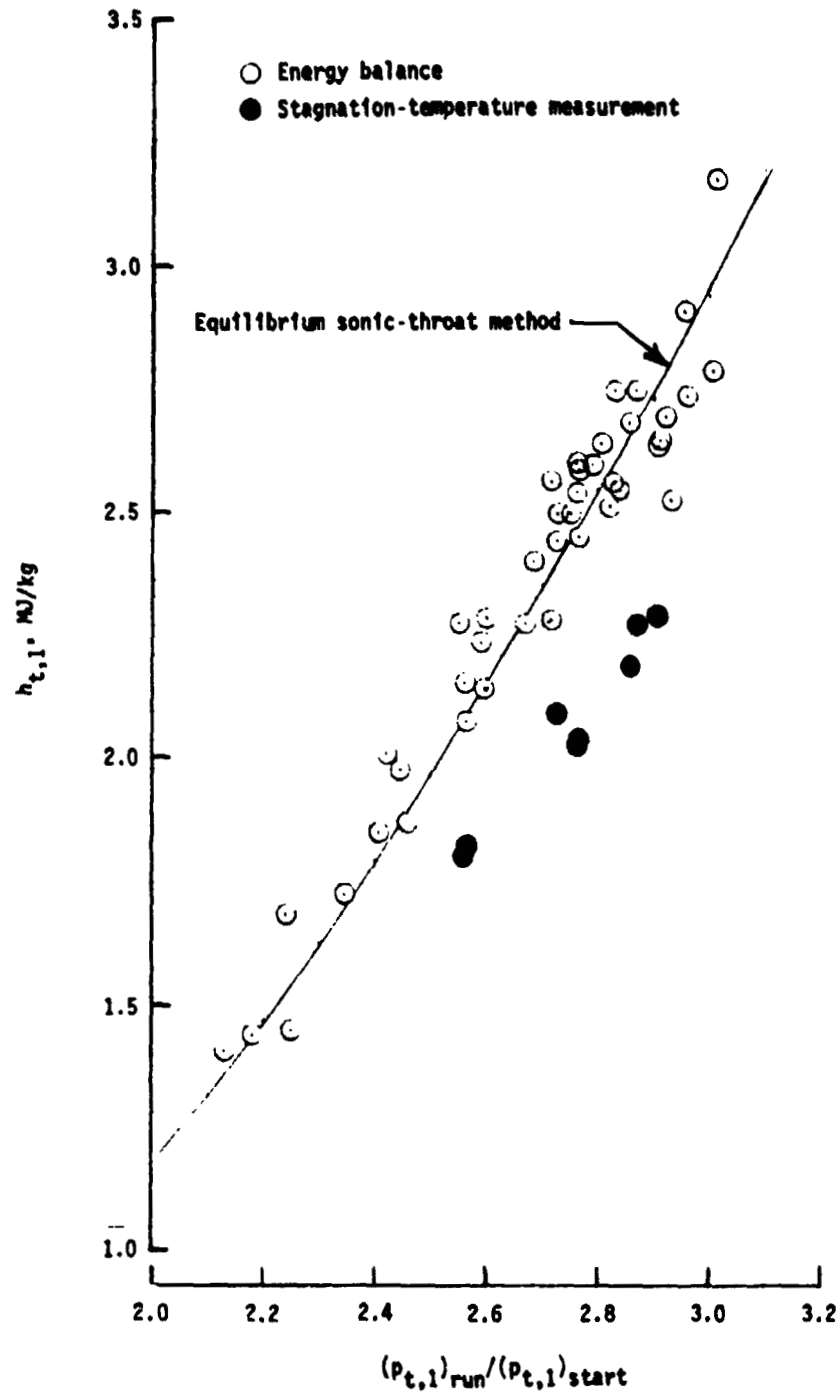

Figure 11.- Comparison of total enthalpy determined by several methods.

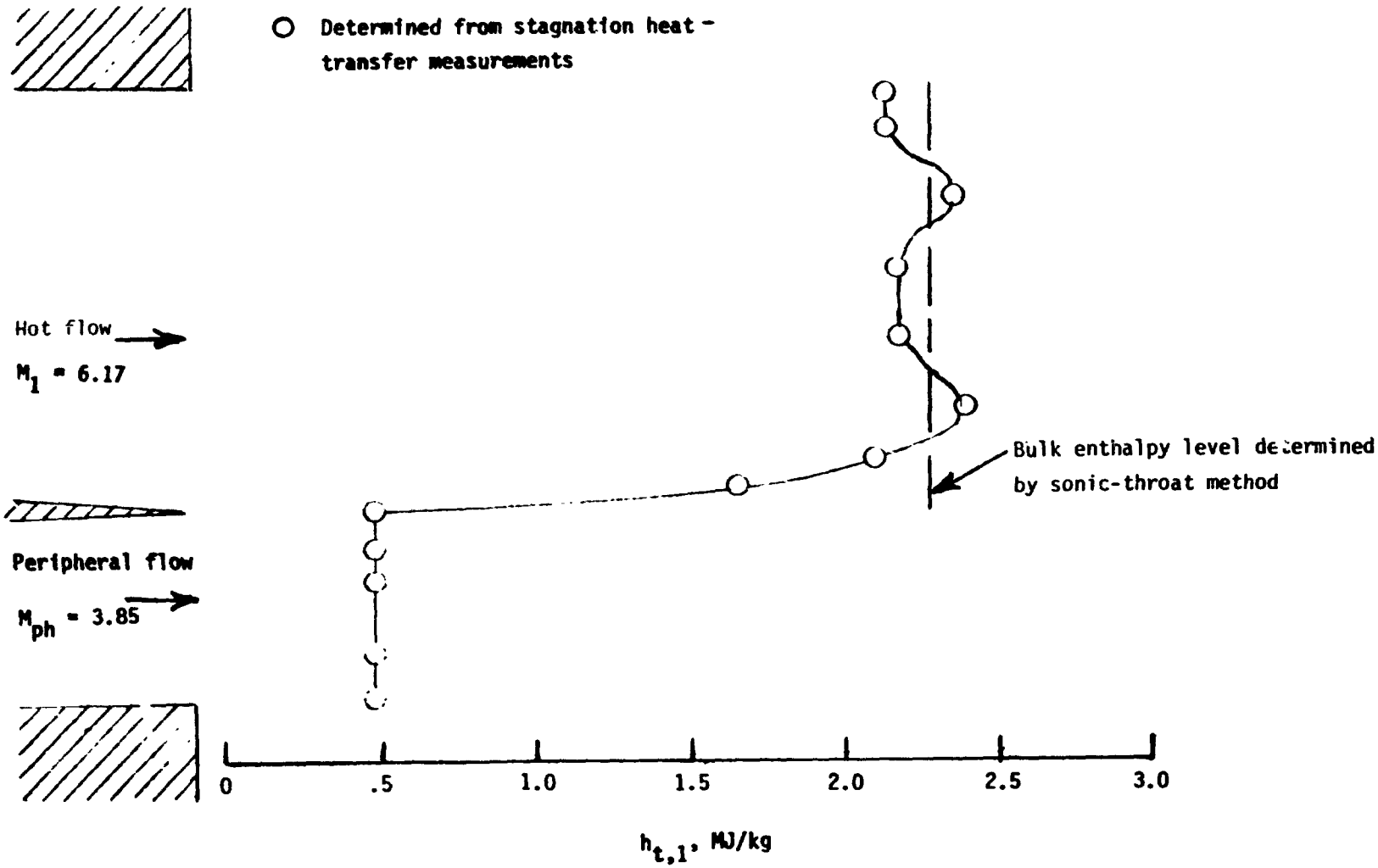

Figure 12.- Air total enthalpy in facility nozzle exit plane.

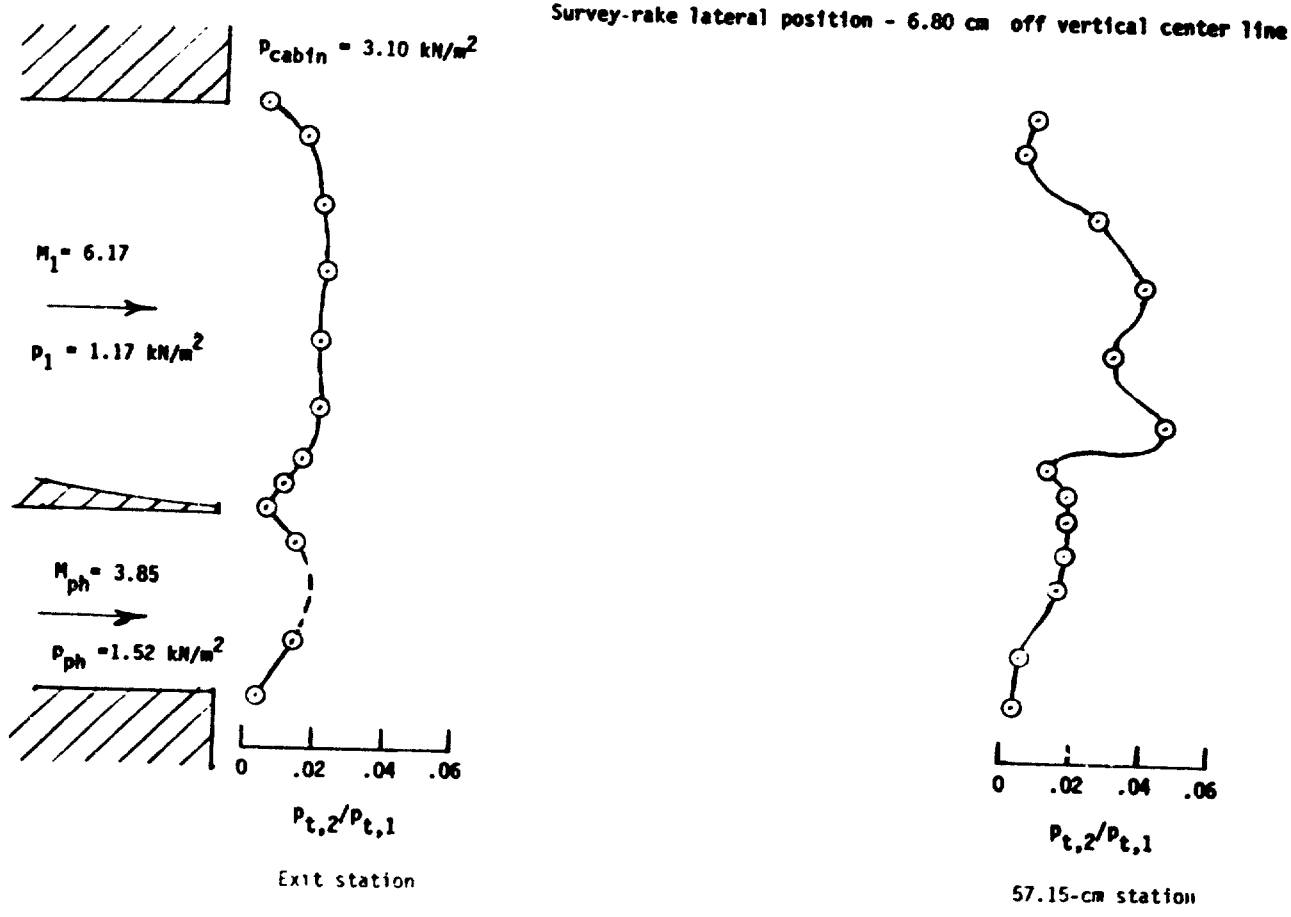

Figure 13.- Pitot-pressure profiles at facility nozzle exit and 57.15-cm station.

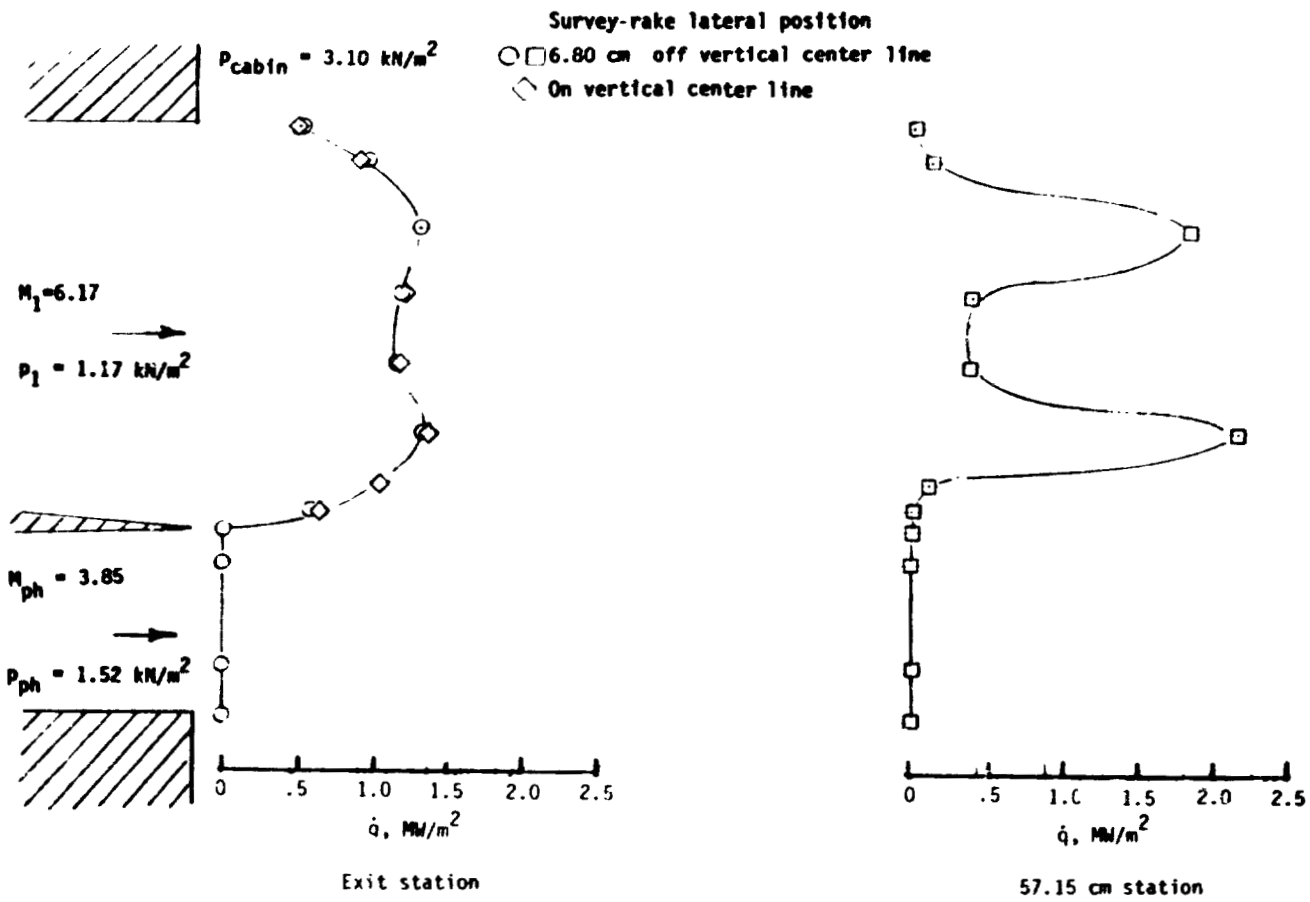

Figure 14.- Stagnation-point heat-transfer-rate profiles at facility nozzle exit and 57.15-cm downstream station.

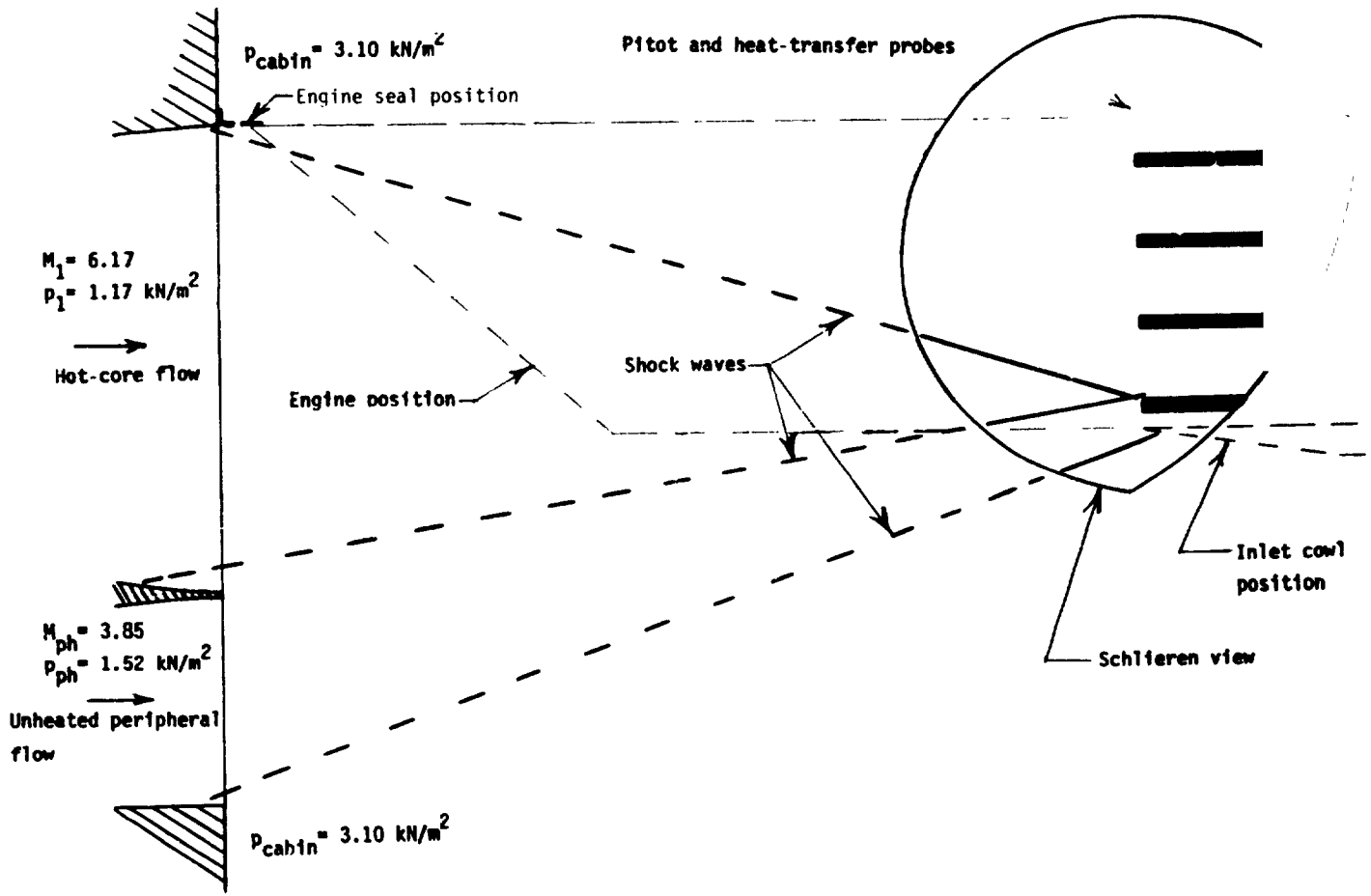

Figure 15.- Test-section flow-field wave diagram.

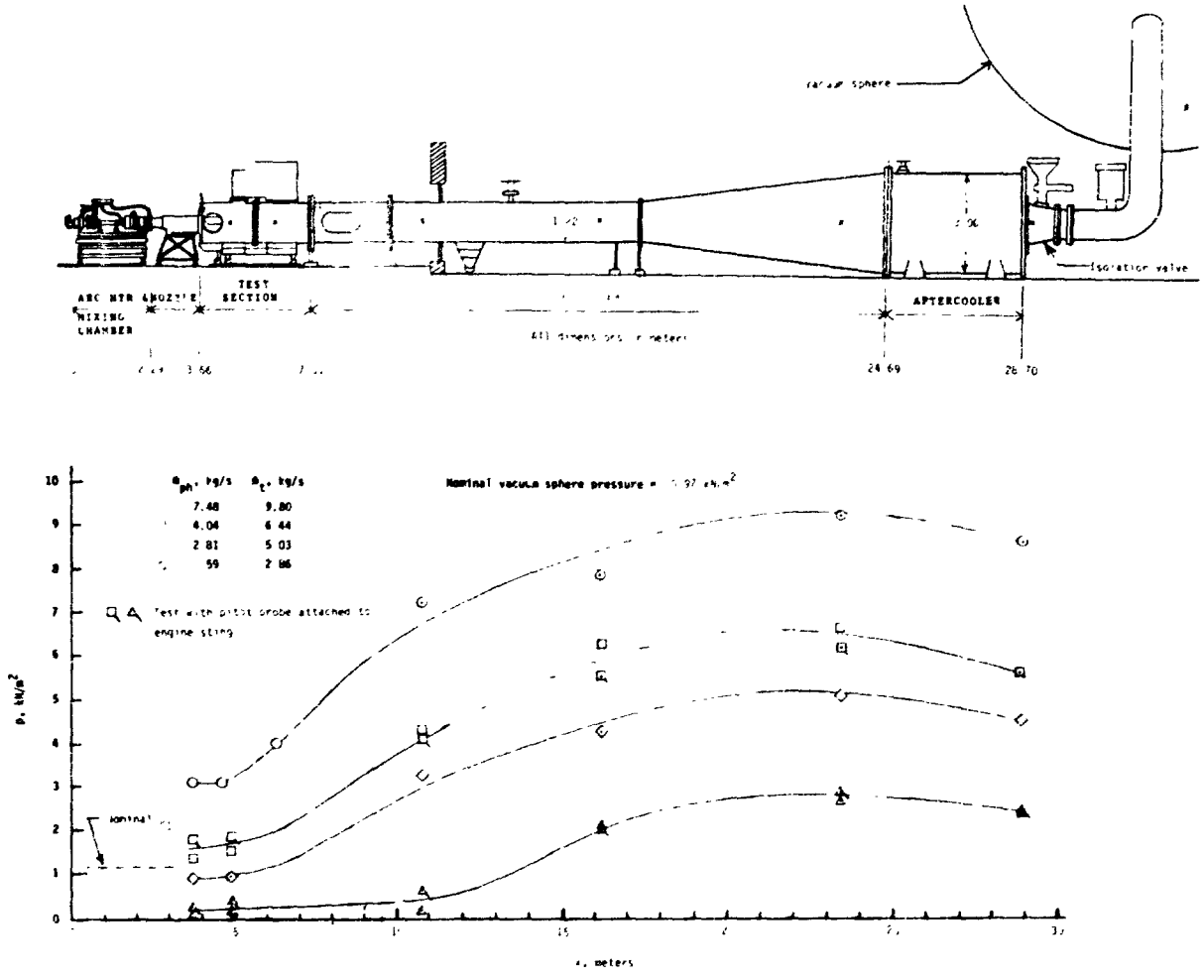

Figure 16.- Effect of peripheral-nozzle airflow rate on test-section and diffuser static-pressure distribution. Dimensions are in meters.

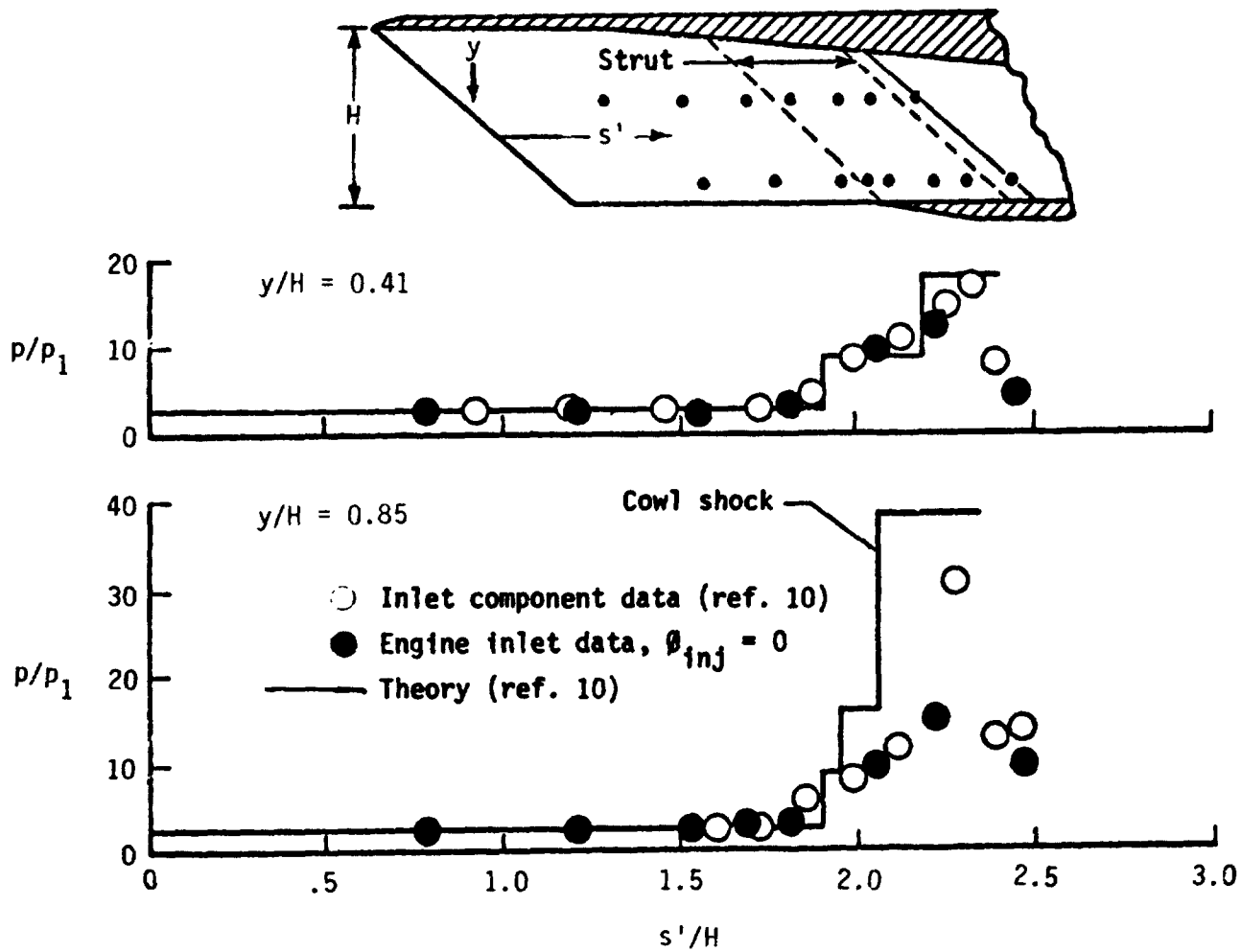

Figure 17.- Verification of inlet start.

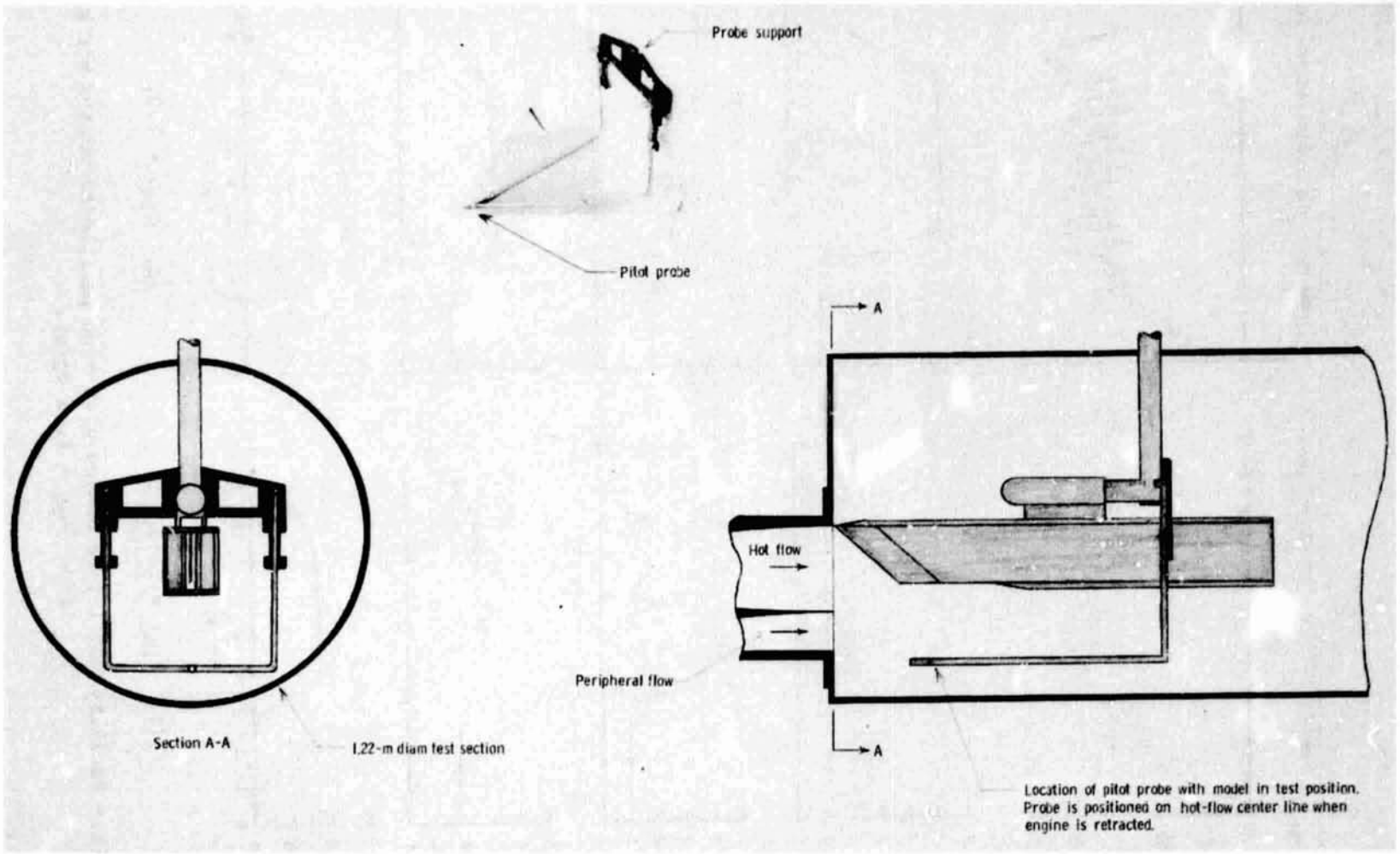

Figure 18.- Scramjet model with pitot probe.

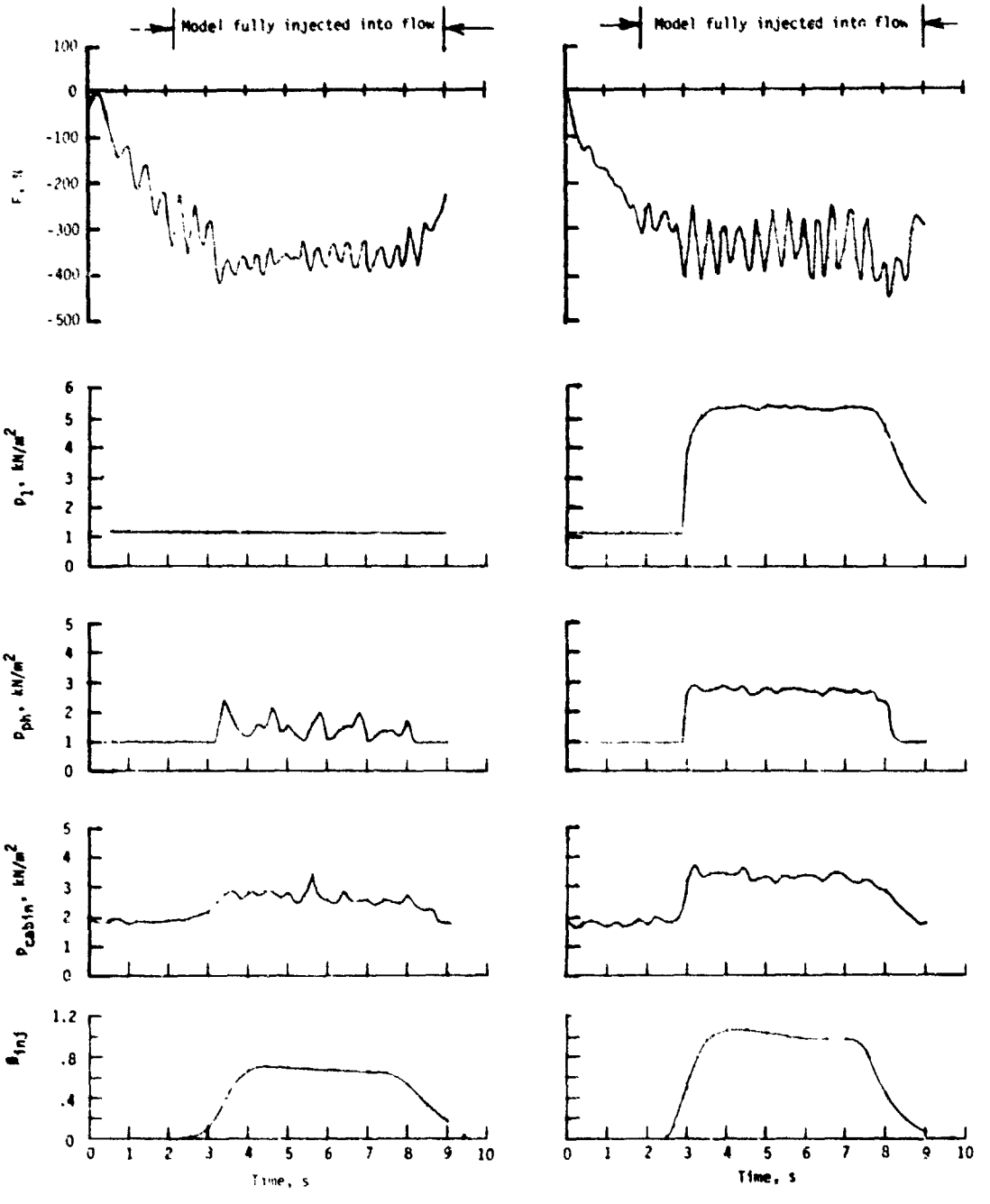

(a) ϕ_{inj} = 0.65. (b) ϕ_{inj} = 1.0.

Figure 19.- Facility-model interaction with high peripheral-nozzle air mass flow ($\dot{m}_{ph}$ = 4.08 kg/s).

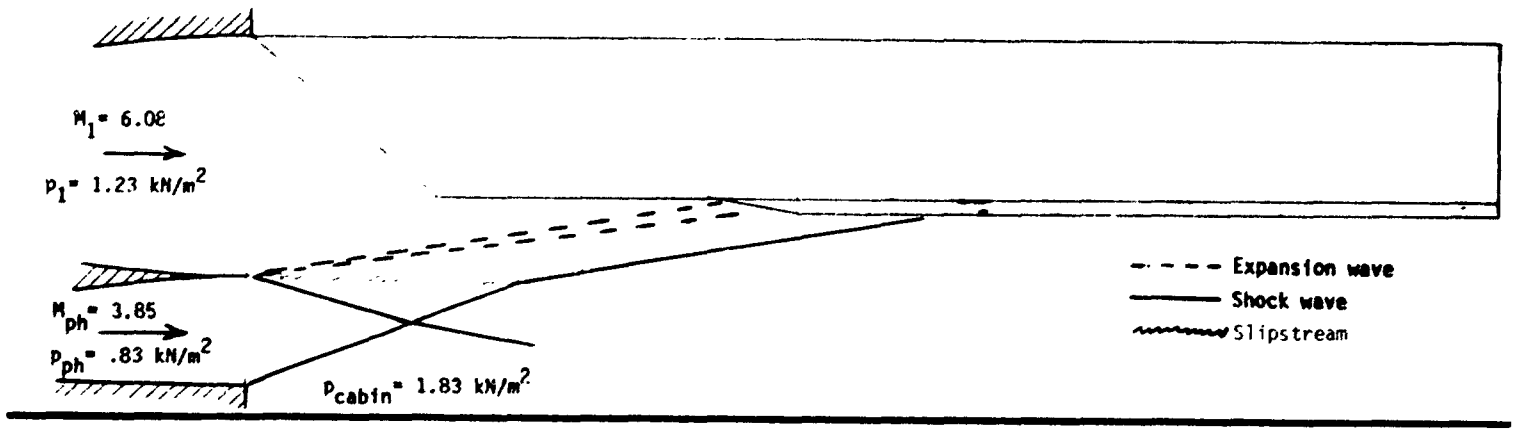

(a) Side view.

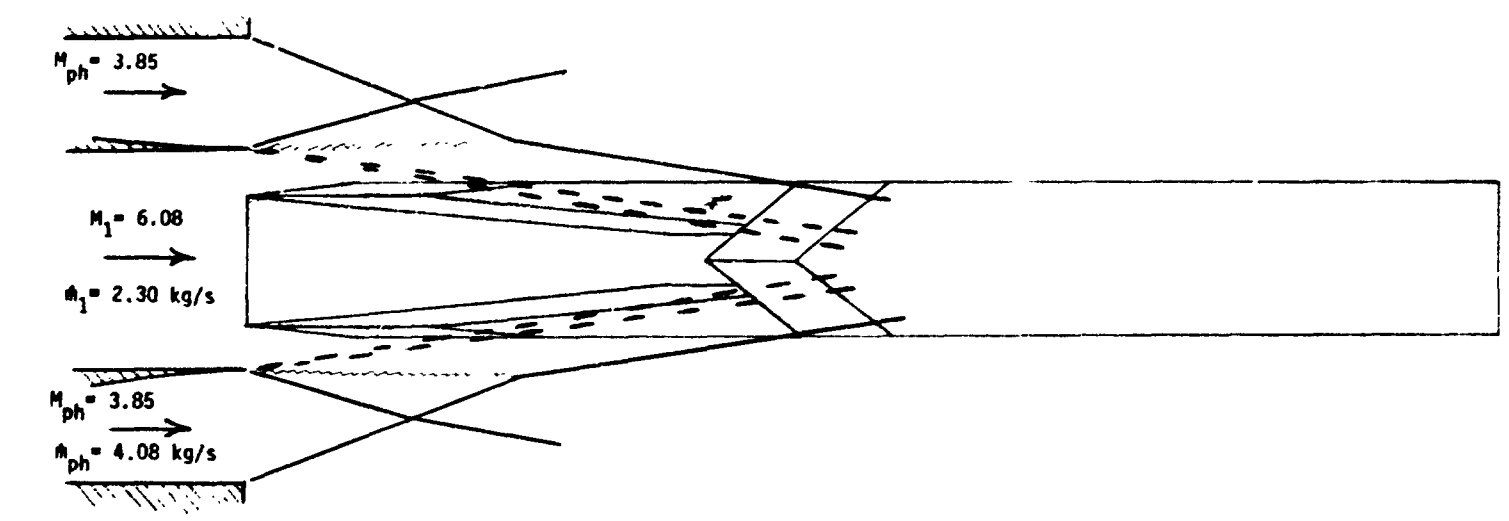

(b) Bottom view.

Figure 20.- Effect of test-section and nozzle exit pressure on wave-system impingement on engine.

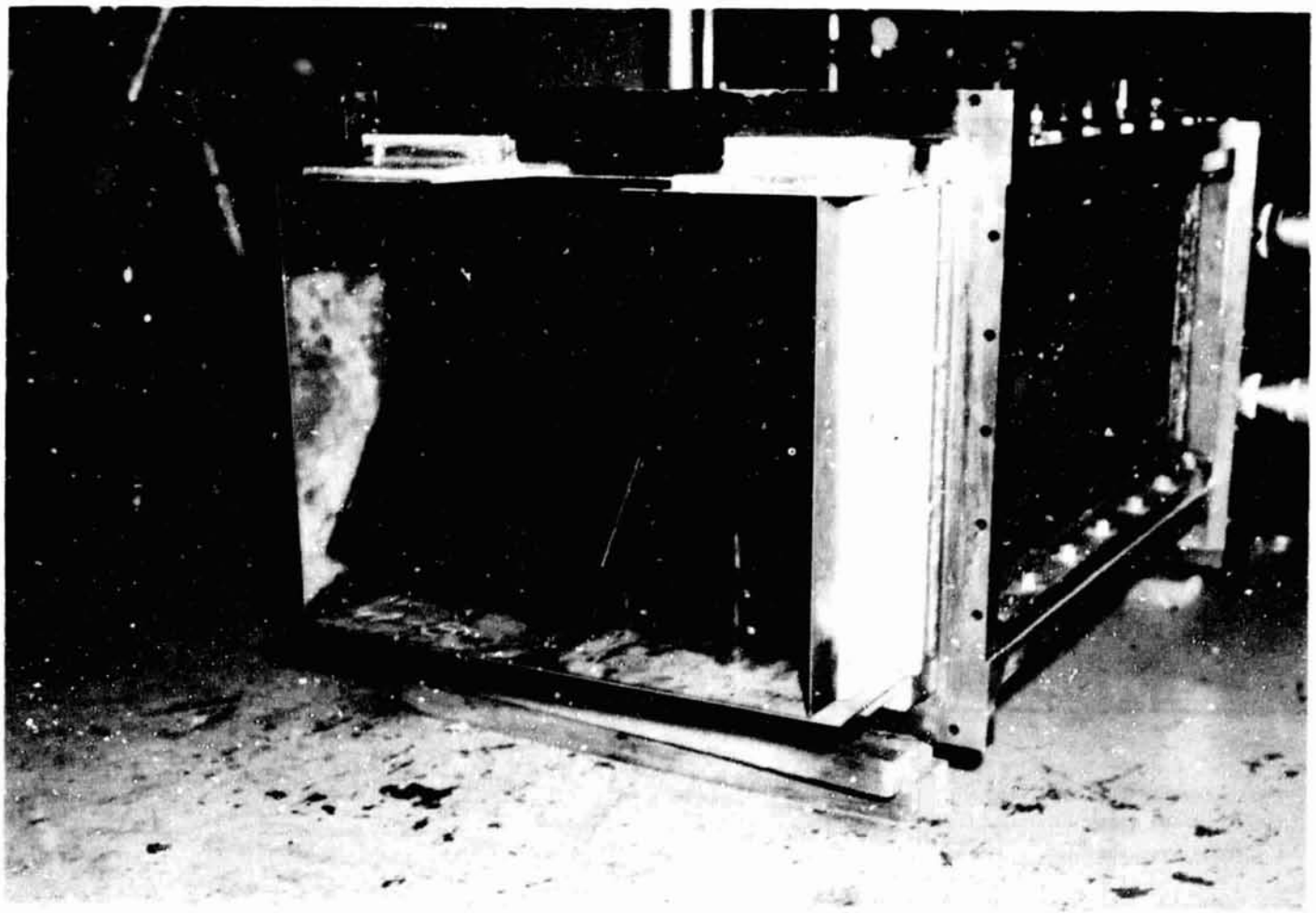

L-76-6511

(a) Removed from facility.

Figure 21.- Facility nozzles with extensions.

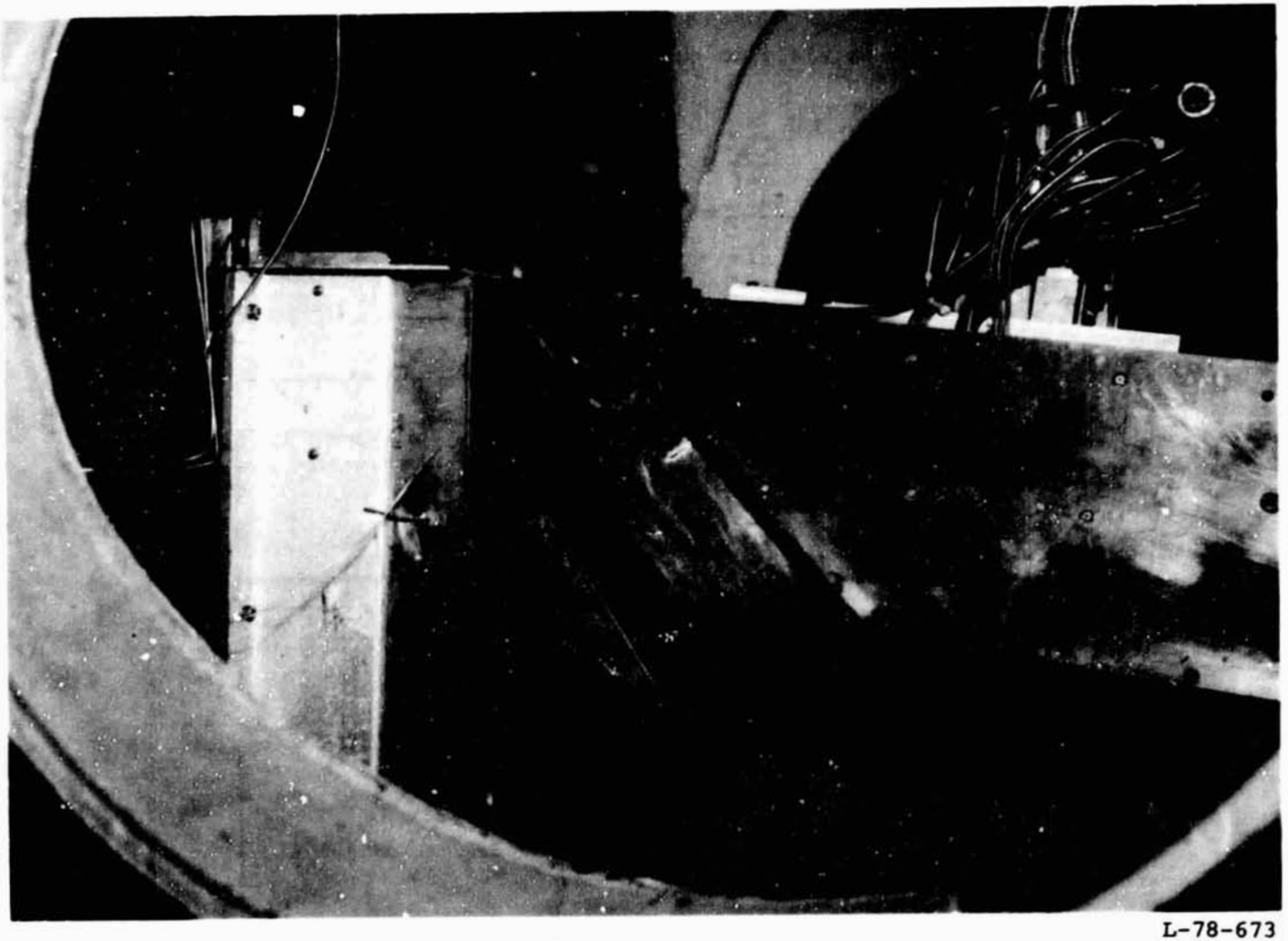

L-78-673

(b) Installed.

Figure 21.- Concluded.

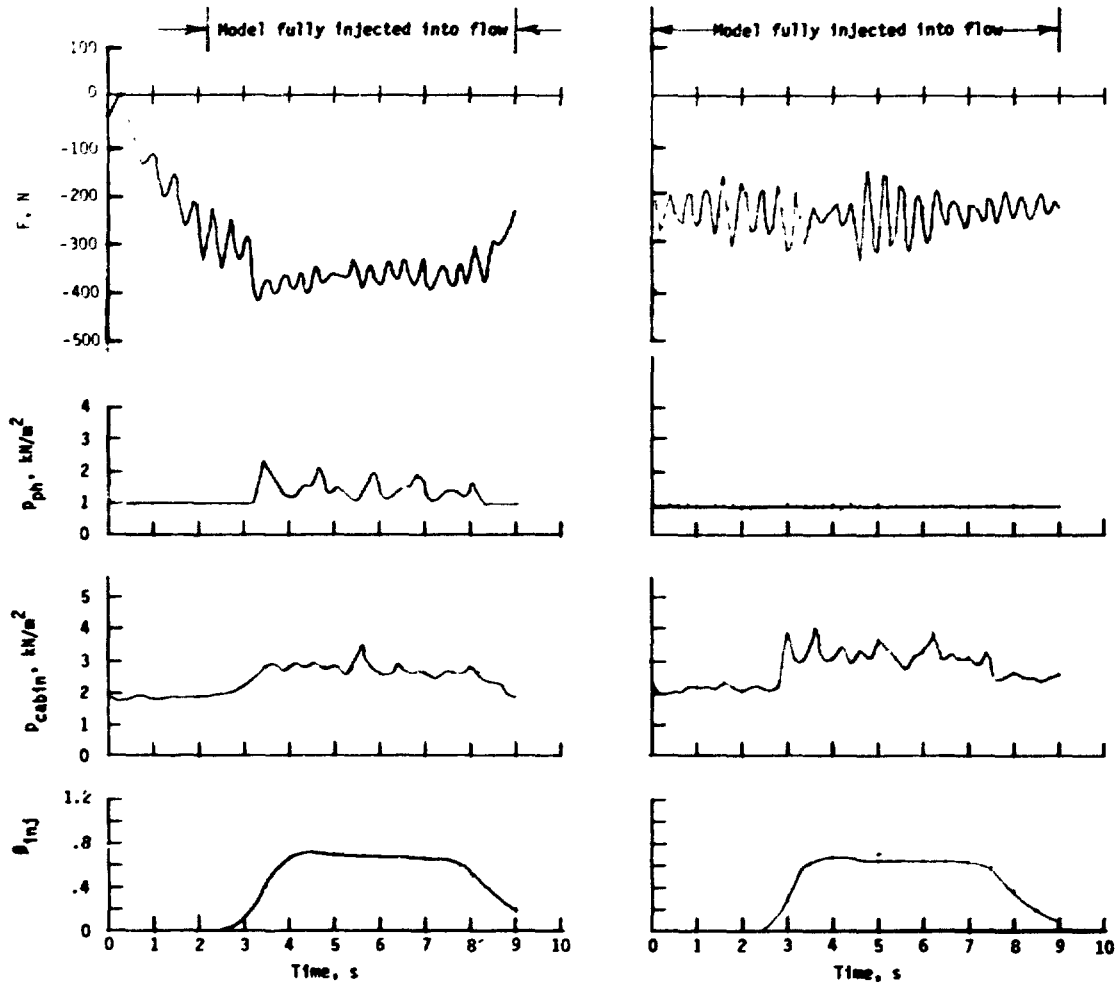

(a) Without extensions.

(b) With extensions.

Figure 22.- Effect of nozzle extensions on facility-model interaction ($\dot{m}_{ph}$ = 4.08 kg/s).

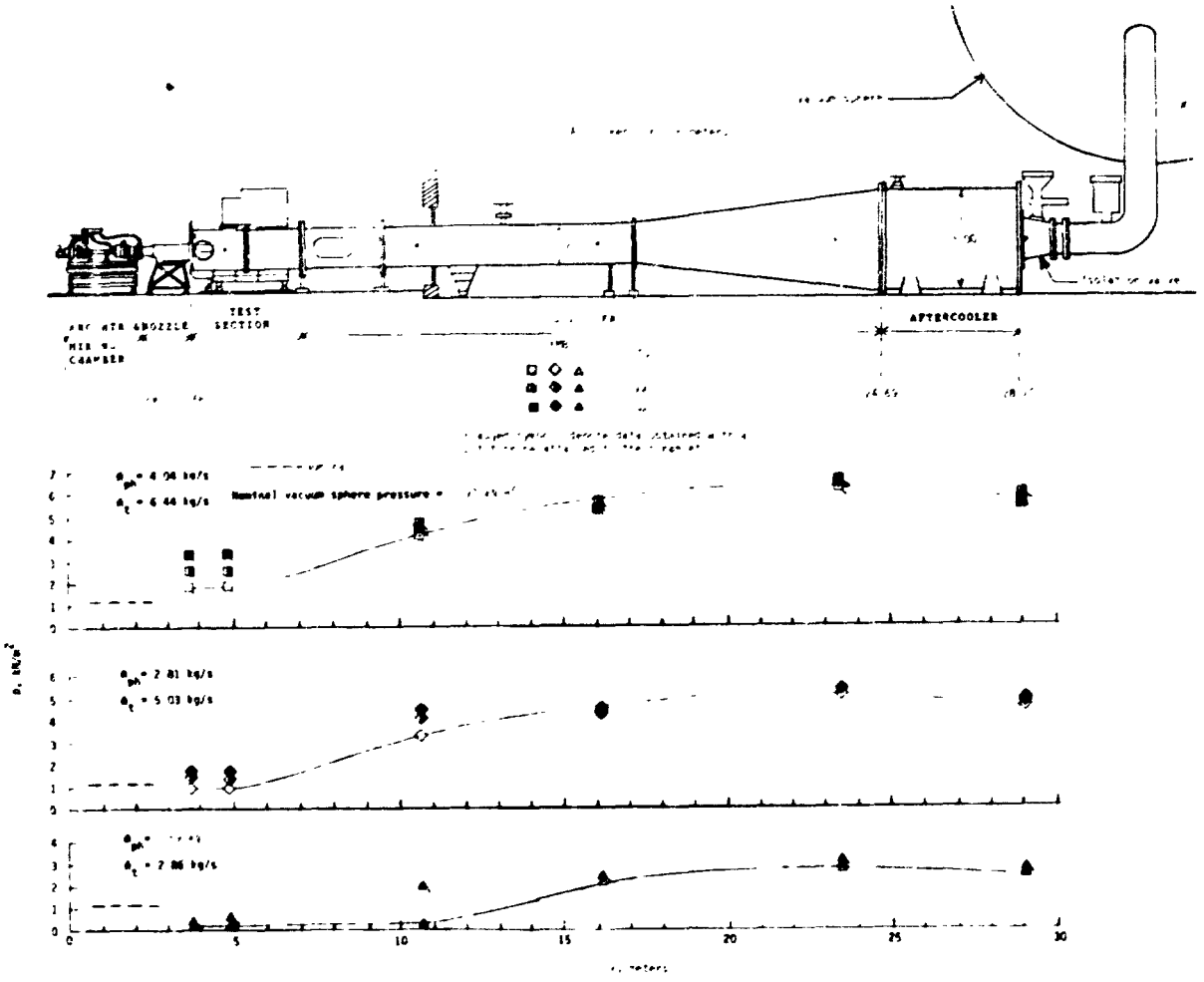

Figure 23.- Effect of fuel injection on test-section and diffuser static pressures at several facility air mass flow rates. Dimensions are in meters.

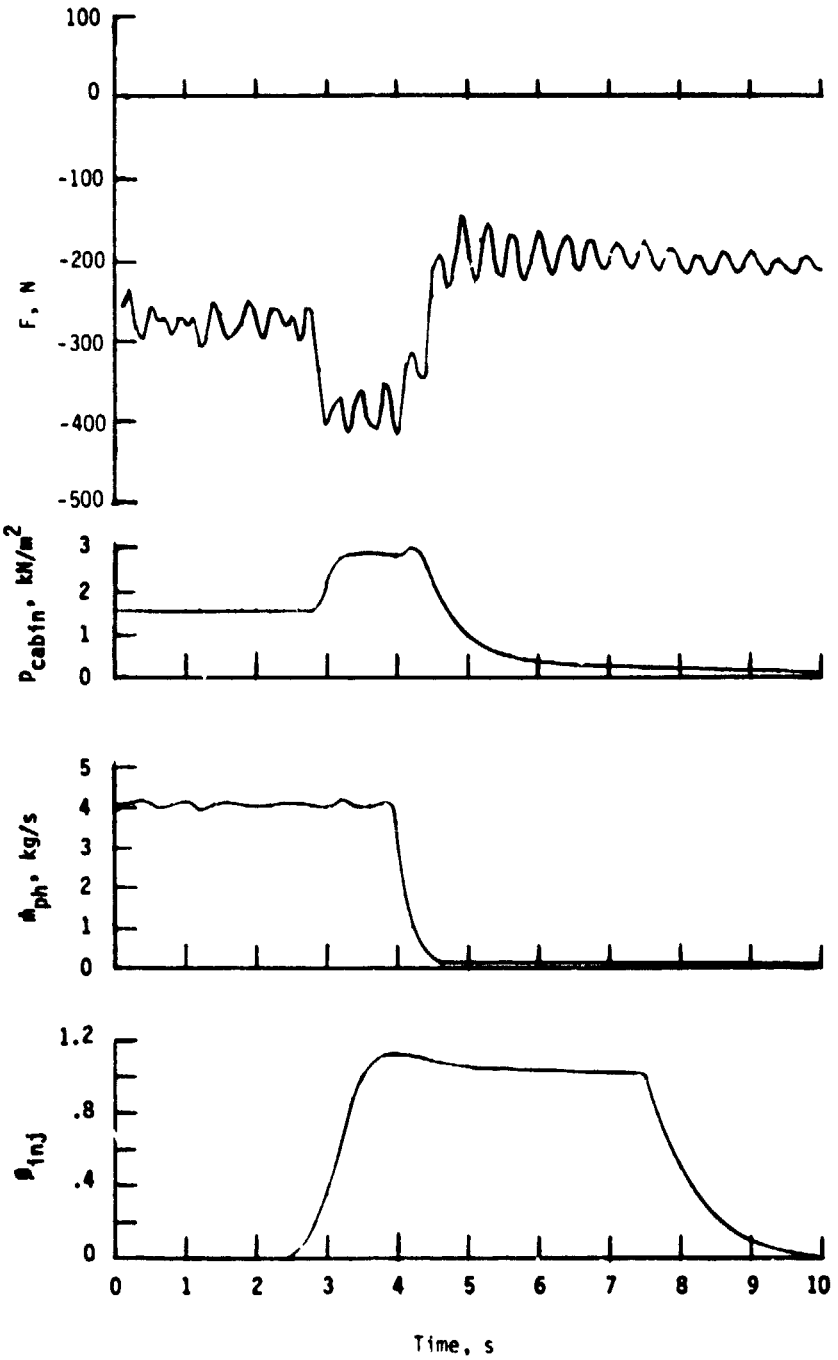

Figure 24.- Effect of peripheral-nozzle airflow rate change on test-cabin pressure and engine drag ($\dot{m}_j$ = 2.30 kg/s).

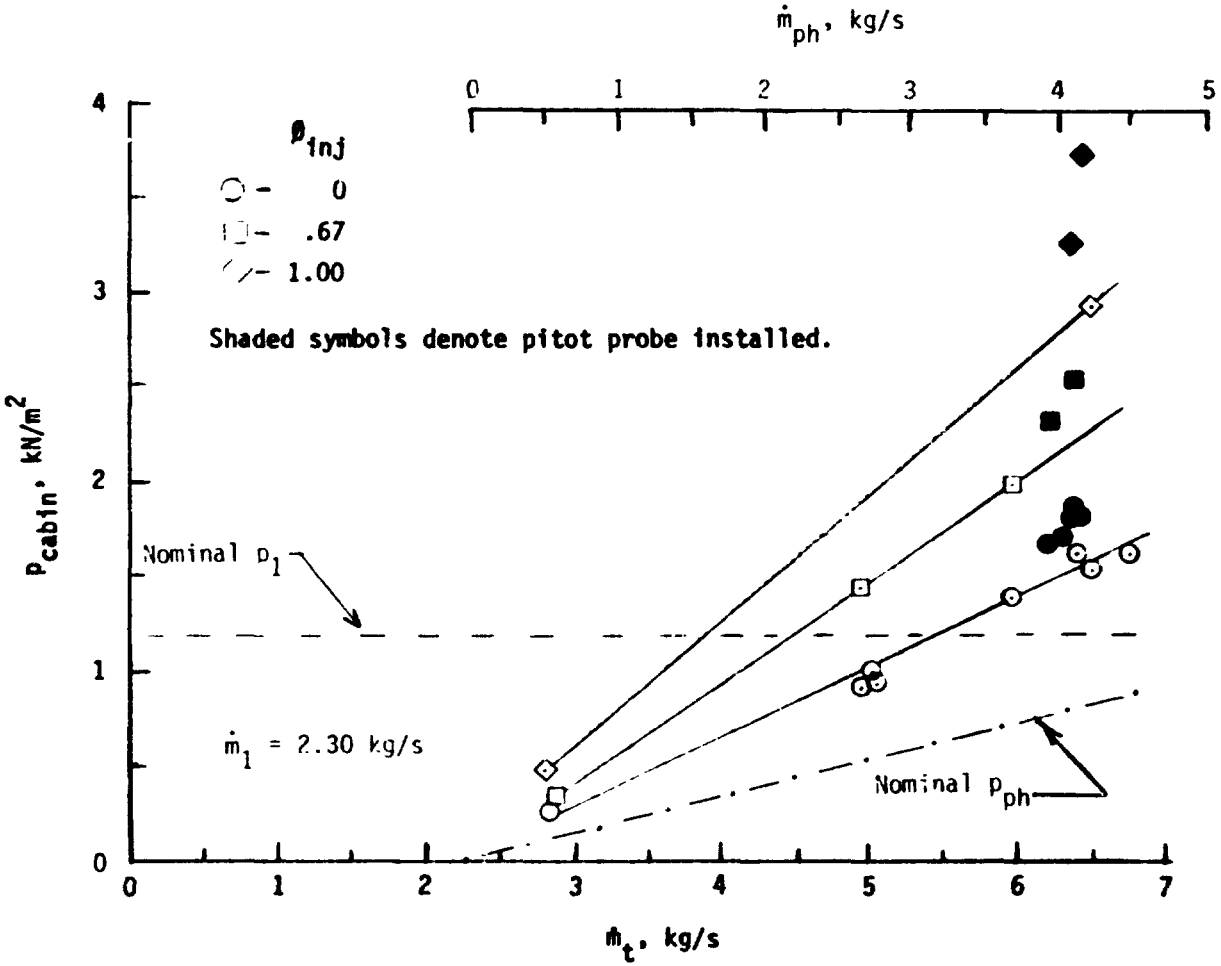

Figure 25.- Test-cabin pressure variation with engine fuel-equivalence ratio and facility airflow rate.

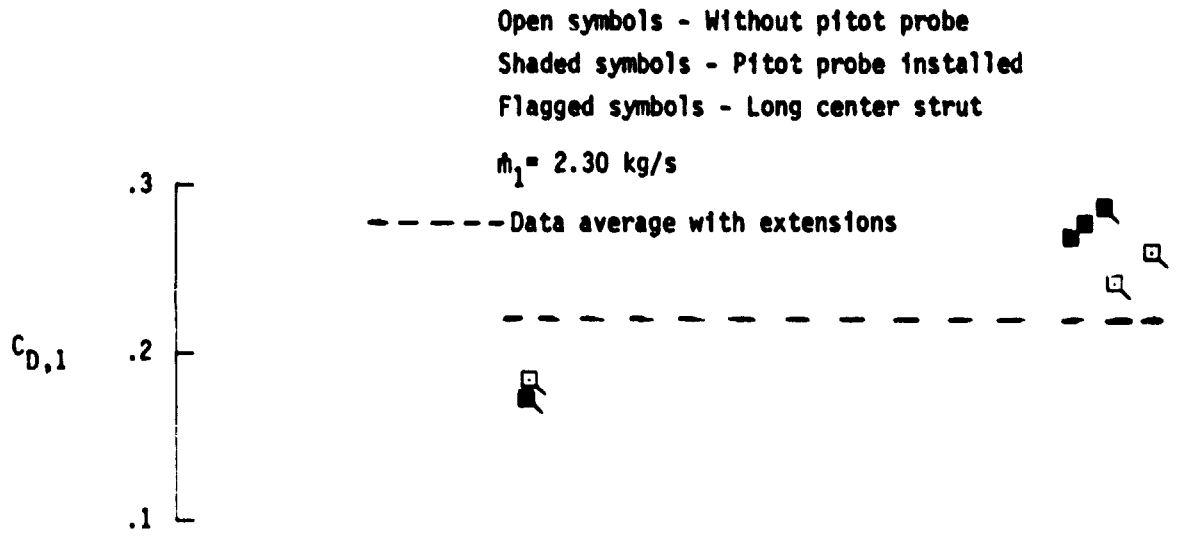

(a) Without nozzle extensions.

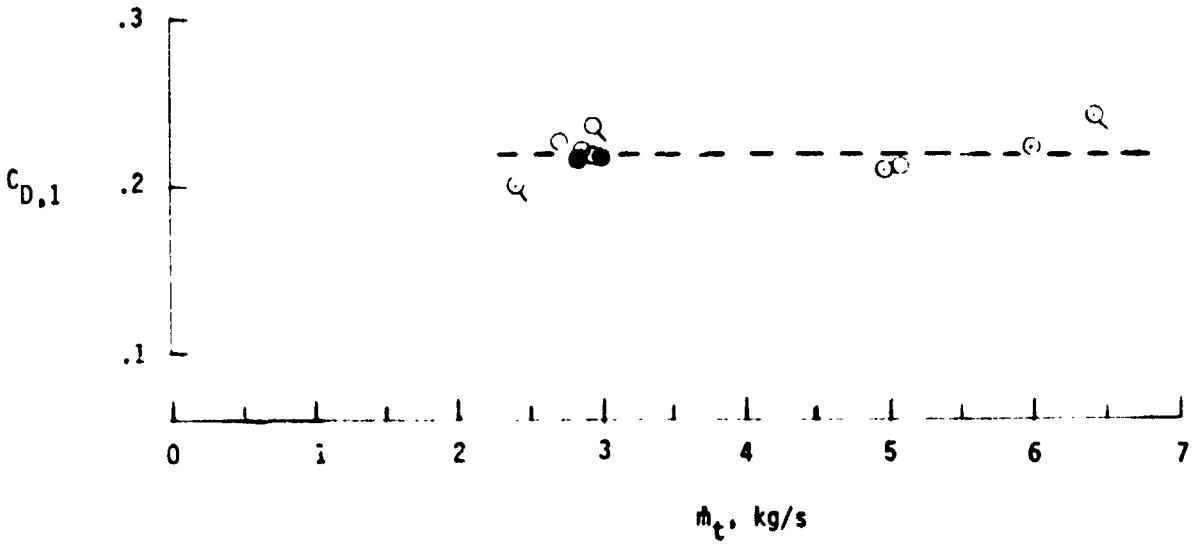

(b) With nozzle extensions.

Figure 26.- Fuel-off engine drag variation with facility air mass flow rate.

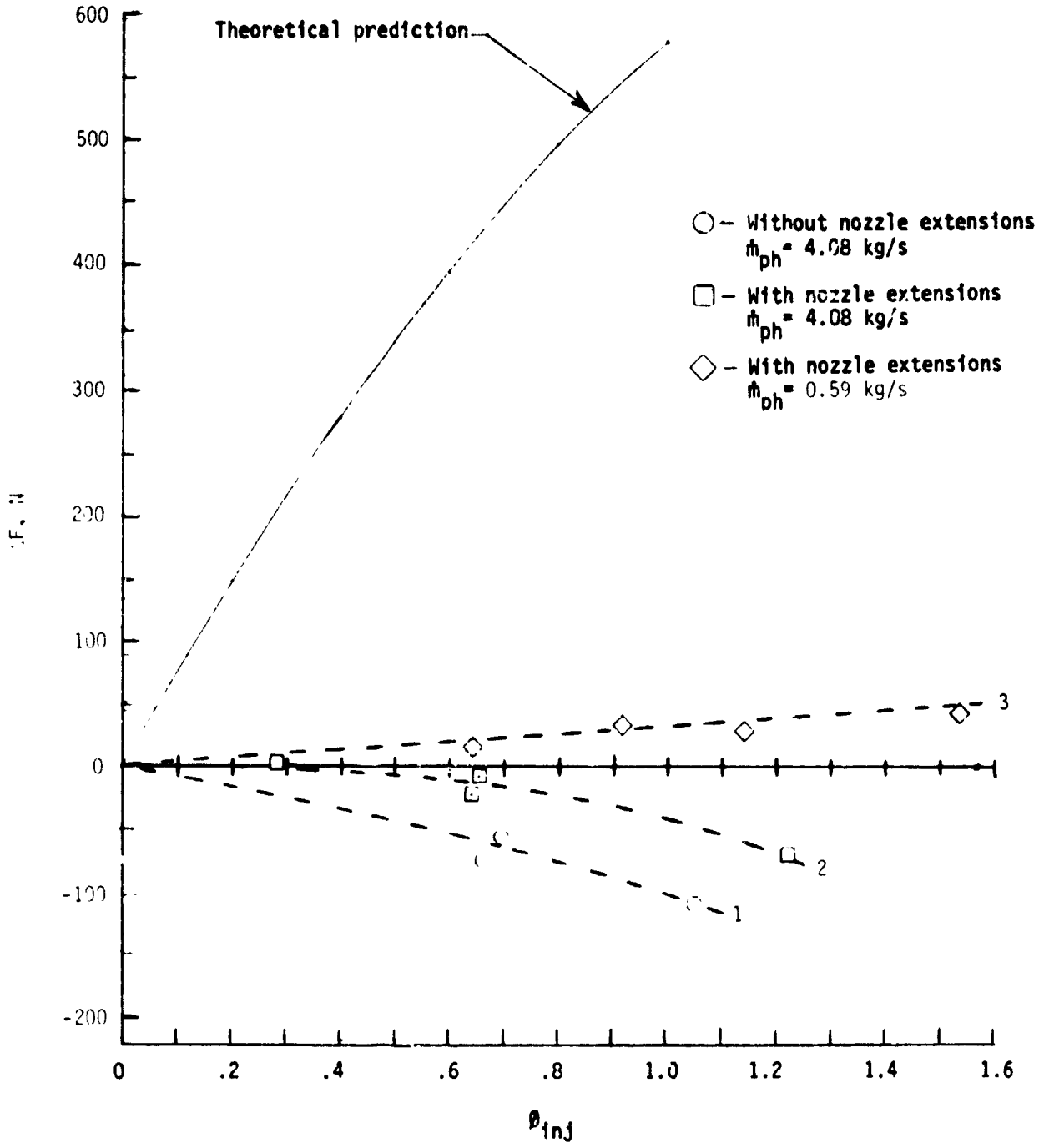

Figure 27.- Summary of scramjet performance illustrating effects of facility-model interaction ($\dot{m}_1$ = 2.30 kg/s).